Secondary Organic Aerosol Formation from Camphene Oxidation: Measurements and Modeling

Qi Li[1,2], Jia Jiang[1,2], Isaac Kwadjo Afreh [1,2], Kelley C. Barsanti[1,2], David R. Cocker III[1,2]

[1]Department of Chemical and Environmental Engineering, University of California-Riverside, Riverside, California 92521, United States
[2]The Bourns College of Engineering, Center for Environmental Research and Technology, University of California-Riverside, Riverside, California 92507, United States

Correspondence to: Kelley C. Barsanti (kbarsanti@engr.ucr.edu) and David R. Cocker III (dcocker@engr.ucr.edu)

Abstract. While camphene is one of the dominant monoterpenes measured in biogenic and pyrogenic biomass burning emissions samples, oxidation of camphene has not been well-studied in environmental chambers and very little is known about its potential to form secondary organic aerosol (SOA). The lack of chamber-derived SOA data for camphene may lead to significant uncertainties in predictions of SOA from oxidation of monoterpenes using existing parameterizations when camphene is a significant contributor to total monoterpenes. Therefore, to advance the understanding of camphene oxidation and SOA formation, and to improve representation of camphene in air quality models, a series of experiments were performed in the University of California Riverside environmental chamber to explore camphene SOA mass yields and properties across a range of chemical conditions at atmospherically relevant OH concentrations. The experimental results were compared with modeling simulations obtained using two chemically detailed box models, Statewide Air Pollution Research Center (SAPRC) and Generator for Explicit Chemistry and Kinetics of Organics in the Atmosphere (GECKO-A). SOA parameterizations were derived from the chamber data using both the two-product and volatility basis set (VBS) approaches. Experiments performed with added nitrogen oxides (NO_x) resulted in higher SOA mass yields (up to 64%) than experiments performed without added NO_x (up to 28%). In addition, camphene SOA mass yields increased with SOA mass (M_o) at lower mass loadings, but a threshold was reached at higher mass loadings in which the SOA mass yields no longer increased with M_o. SAPRC modeling of the chamber studies suggested that the higher SOA mass yields at higher initial NO_x levels were primarily due to higher production of peroxy radicals (RO_2) and the generation of highly oxygenated organic molecules (HOMs) formed through unimolecular RO_2 reactions. SAPRC predicted that in the presence of NO_x, camphene RO_2 reacts with NO and the resultant RO_2 undergo hydrogen (H)-shift isomerization reactions; as has been documented previously, such reactions rapidly add oxygen and lead to products with very low volatility (i.e., HOMs). The end products formed in the presence of NO_x have significantly lower volatilities, and higher O:C ratios, than those formed by initial camphene RO_2 reacting with hydroperoxyl radicals (HO_2) or other RO_2. Further analysis reveals the existence of an extreme NO_x regime, where the SOA mass yield can be suppressed again due to high NO/HO_2 ratios. Moreover, particle densities were found to decrease from 1.47 to 1.30 g cm^{-3} as $[HC]_0/[NO_x]_0$ increased and O:C decreased. The observed differences in SOA mass yields were largely explained by the gas-phase RO_2 chemistry and the competition between $RO_2 + HO_2$, $RO_2 + NO$, $RO_2 + RO_2$, and RO_2 unimolecular autoxidation reactions.

1 Introduction

On a global scale, biogenic monoterpene emissions are estimated to contribute 14% of the total reactive volatile organic compound (VOC) flux (Tg C) (Guenther, 1995). Camphene is an ubiquitous monoterpene emitted from biogenic sources (Geron et al., 2000; Hayward et al., 2001; Ludley et al., 2009; Malekniu et al., 2007; White et al.,

40 2008) and pyrogenic sources (Akagi et al., 2013; Gilman et al., 2015; Hatch et al., 2015). Many studies have reported camphene as a top contributor by mass in measured biogenic and pyrogenic monoterpene emissions (Benelli et al., 2018; Hatch et al., 2019; Komenda, 2002; Mazza & Cottrell, 1999; Moukhtar et al., 2006). For example, in measurements of laboratory and prescribed fires reported by Hatch et al. (2019), camphene was among the top two monoterpenes emitted from subalpine and Douglas fir fires based on emission factors (mass of compound
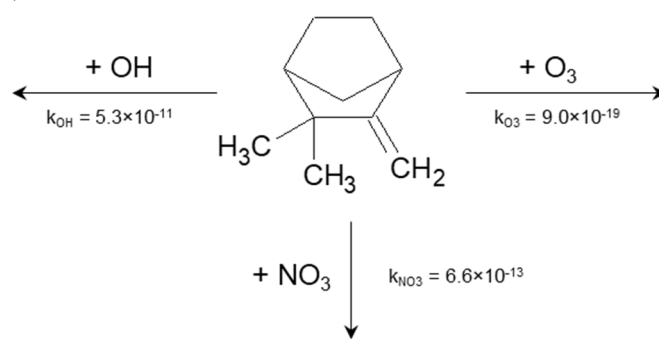
45 emitted/mass of fuel burned).

Figure 1. Camphene chemical structure and reaction rate constants (unit: cm^3 $molecule^{-1}$ s^{-1}) with major atmospheric oxidants.

When emitted to the atmosphere, monoterpenes form oxygenated compounds through reactions with ~~trace~~ oxidants

50 such as hydroxyl radicals (OH), ozone (O_3) and nitrate radicals (NO_3); compounds with sufficiently low volatility can then condense to form secondary organic aerosol (SOA). Figure 1 shows the chemical structure of camphene and its reaction rate constants with major atmospheric oxidants. The SOA formation potential of individual monoterpenes can vary greatly based on their molecular structure, atmospheric lifetimes, and the volatility of their oxidation products (Atkinson and Arey, 2003; Griffin et al., 1999; Ng et al., 2007a; Zhang et al., 1992). Previous experimental studies of

55 other monoterpenes (such as α-pinene, β-pinene, d-limonene, etc.) have reported SOA mass yields from ~10% to 50% through OH oxidation and from ~0 to 65% through NO_3 oxidation; among the studied monoterpenes, d-limonene often has the highest reported yields (Mutzel et al., 2016; Griffin et al., 1999; Ng et al., 2007b; Fry et al., 2014). Few studies have been published regarding camphene SOA formation.

Past experimental studies of camphene largely have been focused on gas-phase reactivity with OH, NO_3, and/or

60 O_3 and gas-phase product identification (e.g., Atkinson et al., 1990; Gaona-Colmán et al., 2017; Hakola et al., 1994). Baruah et al. (2018) performed a kinetic and mechanism study of the camphene oxidation initiated by OH radicals using ~~the~~ density functional theory (DFT), in which the rate constant and atmospheric lifetime were reported. It was also suggested that addition at the terminal double bond carbon atom could account for 98.4% of the initial OH-addition. A product study by Gaona-Colmán et al. (2017) showed obvious NO_x dependence in OH + camphene

experiments, in which the molar yield of acetone was enhanced by a factor of 3, 33% relative to 10%, in the presence of NO_x (2–2.3 ppmv of NO).

Hatfield and Huff-Hartz studied SOA formation from ozonolysis of VOC mixtures, in which the added camphene was considered a non-reactive VOC and assumed to have little to no effect on SOA mass yields (Hatfield & Hartz, 2011). Mehra et al. (2020) recently published a compositional analysis study of camphene SOA. Although SOA mass yields were not provided, they demonstrated the potential contribution of highly oxygenated organic molecules (HOMs) and oligomers to camphene SOA formed in an oxidation flow reactor (OFR). Afreh et al. (2020) presented the first mechanistic modeling study of camphene SOA formation. While relatively high SOA mass yields were reported (with final SOA mass and yields in twice that of α-pinene), no chamber-based SOA data were available for measurement–model comparison at that time.

SOA formation has been shown to be highly dependent on gas-phase NO_x concentrations; and more precisely, the relative ratios of $NO:HO_2$, hydroperoxyl radicals:RO_2, peroxy radicals (Henze et al., 2008; Ng et al., 2007b; Presto et al., 2005; Ziemann and Atkinson, 2012; Kroll and Seinfeld, 2008; Song et al., 2005). During chamber experiments, VOCs are subject to oxidation by OH, O_3 and/or NO_3. For some precursors, NO_x levels influence the amount of SOA produced in the initial oxidation steps by controlling the relative proportions of oxidants, the fractional reactivity with those oxidants, and thus the volatility distribution of the products formed (Hurley et al., 2001; Nøjgaard et al., 2006; Kroll and Seinfeld, 2008). For other precursors, NO_x levels influence the amount of SOA produced via fate of RO_2. The reactions between RO_2 and HO_2 form hydroperoxides, which can have sufficiently low volatility to condense into the particle phase. In the presence of NO_x, RO_2 will react with NO, forming organic nitrate and carbonyl compounds that have higher volatilities than the products formed through the HO_2 pathway (Kroll and Seinfeld, 2008; Ziemann and Atkinson, 2012). Previous studies of relatively small compounds (carbon number ≤10), including monoterpenes such as α-pinene, have reported that SOA mass yields generally increase as initial NO_x decreases, with a proposed mechanism of competitive chemistry between $RO_2 + HO_2$ and $RO_2 + NO$ pathways, of which the latter would form more volatile products (Kroll et al., 2006; Ng et al., 2007; Song et al., 2005). The NO_x dependence of camphene oxidation and SOA formation has been relatively understudied.

The atmospheric gas-phase autoxidation of RO_2 has been identified as another key pathway of SOA formation (Crounse et al., 2013; Jokinen 2014; Ehn et al., 2017; Bianchi et al., 2019). The RO_2 radical undergoes intramolecular H-atom abstraction reactions to form a hydroperoxide functionality and an alkyl radical (RO), to which a new RO_2 will be formed by adding O_2. The autoxidation process can repeat several times until terminated by other pathways and will form low-volatility compounds known as highly oxygenated organic molecules (HOMs) (Bianchi et al., 2019). Recent theoretical and experimental studies have been conducted to understand HOM formation from monoterpenes such as α-pinene and β-pinene (Zhang et al., 2017; Quéléver et al., 2019; Xavier et al., 2019; Pullinen et al., 2020; Ye et al., 2020), but the potential importance and mechanisms of HOM formation from camphene have not been well investigated.

Here, we present the first systematic study of SOA -formation from camphene using laboratory-based chamber experiments and chemically detailed box models. The experiments were conducted at varying NO_x levels and the chamber data were used to provide SOA parameterizations based on the two-product (Odum et al., 1996) and volatility basis set (VBS) modeling approaches (Donahue et al., 2006; Donahue et al., 2009). Two chemically detailed box models, Statewide Air Pollution Research Center (SAPRC) and Generator for Explicit Chemistry and Kinetics of Organics in the Atmosphere (GECKO-A), were used to provide mechanistic insights into the chamber observations and to elucidate the connections between the fate of RO_2, HOM forming mechanisms, and camphene SOA formation.

2 Methods

2.1 Chamber Facility and Instrumentation

The camphene photooxidation experiments were conducted in the University of California, Riverside (UCR) dual indoor environmental chamber. Chamber characterization and features have been previously described in detail (Carter et al., 2005). Briefly, the UCR environmental chamber consists of two 90 m³ collapsible Teflon reactors (2milMIL (0.0508 mm) FEP film) kept at a positive pressure differential (0.0153.73–4.980.020 in H₂OPa) to the enclosure where the reactors are located to minimize contamination during experiments. The enclosure is relative humidity controlled (<0.1%), temperature controlled (300 ± 1 K), and continuously flushed with dry purified air (dew point < -40 °C). Prior to and between experiments, reactors were collapsed to a volume < 20 m³ for cleaning. The cycle of filling-purging the reactors was repeated until particle number concentrations were < 5 cm⁻³ and NO_x mixing ratios were < 1 ppb. The reactors were then flushed with dry purified air and filled up to 90 m³ overnight. The filling-purging of the reactors is controlled by an "elevator" program in LabView.

NO and NO_2 mixing ratios were monitored by a Thermo Environmental Instruments Model 42C chemiluminescence NO_x analyzer. O_3 mixing ratios were monitored by a Dasibi Environmental Corp. Model 1003-AH O_3 analyzer. An Agilent 6890 gas chromatograph with flame ionization detector (GC-FID) was used to measure the camphene levels during the experiments.

Multiple instruments were used for particle-phase monitoring. Each reactor was equipped with a scanning mobility particle sizer (SMPS), including a TSI 3081 differential mobility analyzer (DMA), to measure the particle mass concentration. Particle wall loss corrections were performed following the method described in Cocker et al. (2001). Vapor wall loss of organics has been reported in multiple chambers (e.g., Zhang et al., 2015, 2014; Schwantes et al., 2019). In the UCR chamber, vapor wall loss has been investigated in SOA experiments using various precursor compounds (including α-pinene and m-xylene) under seed and no seed conditions (Clark et al., 2016; L. Li et al., 2015); no measurable differences in SOA formation have been observed in any of these experiments indicating negligible vapor wall losses. In this work, stability tests on camphene also resulted in negligible vapor wall loss of the parent compound. Thus, the assumption of negligible vapor wall loss was maintained for these experiments. It is noted that this assumption does not affect the major conclusions regarding the role of gas-phase chemistry on SOA formation. The UCR chamber was characterized to show negligible vapor wall losses of running oxidation of compounds (such as α-pinene and m-xylene) under seed and no seed experimentsSemi-volatile vapor wall losses were

~~assumed to be negligible based on previous measurements made during similar experiments in the UCR CE-CERT chamber of other compounds (such as α-pinene and m-xylene), in which negligible differences were observed between seed and no-seed experiments (Clark et al., 2016; L. Li et al., 2015). In addition,~~S~~ stability tests on camphene~~ ~~also resulted in negligible vapor wall loss of the parent compound. The consideration of vapor wall loss doesn't affect the~~

140 ~~conclusions of the study, and we keep the negligible vapor wall loss assumption in the following sections.~~ Particle effective density was directly measured by an Aerosol Particle Mass Analyzer (APM, Kanomax) with a SMPS built in -house (Malloy et al., 2009). Chemical composition of SOA was measured using HR-ToF-AMS (DeCarlo et al., 2006) and analyzed to obtain O:C and H:C ratios by applying the method of Canagaratna et al. (2015). Data processing was performed using the ToF-AMS Analysis Toolkit 1.57 and PIKA 1.16 on Igor Pro 6.36. <u>Based on a prior</u>

145 <u>characterization of this UCR chamber system (Li et al., 2016), the experimental uncertainty in measured SOA yield is < 6.65%.</u>

2.2 Experimental Conditions

A series of 13 <u>camphene</u> photooxidation experiments ~~of camphene~~ were carried out under varying levels of camphene and NO$_x$ ~~with modeling simulations accordingly~~ (Table 1). Due to the relatively high melting point of camphene

150 (51 °C), camphene (Sigma-Aldrich, purity > 96 %, FG) was injected into a glass manifold (heated to 50 °C by heating tape) using a preheated (~50-55 °C) microliter syringe. As camphene evaporated it was carried to the reactors by dry purified compressed air flowing through a glass manifold at 8 LPM for 15 mins. Injection lines from the glass manifold to the reactors were also heated to reduce losses of camphene. H$_2$O$_2$ (Sigma Aldrich, 50 wt.% in H$_2$O) was injected by adding 200 μl onto glass wool in glass tubing and then placing the tubing in a 56 °C oven with 10 LPM of dry

155 purified compressed air flowing through the tubing for 15 mins and into the reactors. An inert tracer, perfluorohexane (Sigma-Aldrich, 99 %) or perfluorobutane (Sigma-Aldrich, 99 %), was injected to the reactors through the heated glass manifold by a carrier gas of 50 °C pure N$_2$. NO (Matheson, UHP) at known volume and pressure was transferred and injected through the same glass manifold as the inert tracer. When gaseous injection of camphene, H$_2$O$_2$, inert tracer, and NO (when used) was completed, the reactors were internally mixed using built-in blowers to ensure uniform

160 distribution of chemicals, and then irradiated using UV black lights (115w Sylvania 350BL) to start photooxidation. No seed aerosol was used in this study. All experiments were conducted under dry conditions (relative humidity < 0.1 %) at 300 K. The initial conditions of the experiments are summarized in Table 1.

Table 1. -Summary of initial conditions for chamber experiments and box model simulations.

	Expt.	Initial Conditions for Chamber Experiments and SAPRC Simulations				Initial Conditions for GECKO-A Simulations			
		Camphene (ppb)	Added NO$_x$ (ppb)	*H$_2$O$_2$ (ppb)	HC/NO$_x$ (ppb/ppb)	Camphene (ppb)	NO$_x$ (ppb)	H$_2$O$_2$ (ppb)	HC/NO$_x$ (ppb/ppb)
without NO$_x$	WO1	7		854		10		1000	
	WO2	9		1148					
	WO3	28		1212		25		1000	
	WO4	57		1182		50		1000	
	WO5	120		1212		100		1000	
	WO6	223		1576		150		1000	
with NO$_x$	W1	7	89	854	0.08	10	80	1000	0.13
	W2	25	138	1040	0.18	25	80	1000	0.31
	W3	32	62	1136	0.51				
	W4	43	7	860	5.91	50	80	1000	0.63
	W5	60	94	1227	0.64				
	W6	131	98	1167	1.33	100	80	1000	1.25
	W7	172	60	1121	2.88	150	80	1000	1.88

165   * H$_2$O$_2$ mixing ratio was targeted at 1ppm but corrected based on tracer (perfluorohexane or perfluorobutane) concentration to offset initial reactor volume bias. Corrected H$_2$O$_2$ mixing ratios were used in SAPRC modeling.

2.3 Model Configurations and Conditions

The chamber experiments were modeled using two different box models, SAPRC and GECKO-A. The SAPRC model was chosen because it has been designed to evaluate gas-phase chemistry in the UCR chamber. The GECKO-A model

170   was chosen because of the ability to predict both gas and particle phase composition, and the prior work of Afreh et al. (2020), in which GECKO-A was used to study SOA formation from camphene. The initial conditions of the simulations are summarized in Table 1.

2.3.1 SAPRC

A gas-phase oxidation mechanism was derived using the SAPRC mechanism generation system (MechGen) with

175   modified initial rate constants (camphene with OH, NO$_3$ and O$_3$) based on published literature data (Atkinson and Arey, 2003Atkinson et al., 1990). MechGen, described elsewhere (Carter, 2021; Carter, 2020b; Jiang et al., 2020), is capable of generating fully explicit mechanisms for the atmospheric reactions of many types of organic compounds and the intermediate radicals they form. MechGen uses experimentally derived rate constants and branching ratios if data are available and otherwise uses estimated rate constants and branching ratios based on group additivity and other

180   estimation methods. This system was used to derive reactions of explicit and lumped organic compounds and products in the development of the SAPRC-18 mechanism (Carter, 2020a) and a detailed SAPRC furans mechanism (Jiang et al., 2020).

     The MechGen-derived camphene mechanism was implemented into the SAPRC box model to simulate chamber experiments under the same chemical conditions as the chamber experiments, where the initial hydrocarbon

concentrations and NO_x levels were as defined in Table 1. The SAPRC box model system has been used for chemical mechanism development, evaluation, and box modeling applications since the mid-1970s (Carter, 1990, 1994, 2000, 2010a, 2010b, 2020a). The initial conditions and relevant chemical parameters for environmental chamber experiments are required inputs; simulations can be performed using multiple versions of the SAPRC gas-phase chemical mechanism. In this work, the recently published version, SAPRC-18 (Carter, 2020a), was selected as the base mechanism because it represents the current state of the science and includes the most up-to-date model species and explicit representation of RO_2 chemistry.

2.3.2 GECKO-A

GECKO-A is a nearly explicit mechanism generator and SOA box model. GECKO-A relies on experimental data and structure-activity relationships (SARs) to generate detailed oxidation reaction schemes for organic compounds. The generated reaction schemes are applied in the SOA box model to simulate SOA formation based on the absorptive gas/particle partitioning model of Pankow (1994), where thermodynamic equilibrium between the gas and an ideal particle phase is assumed. Detailed descriptions of GECKO-A, including mechanism generation and SOA formation, are provided by Aumont et al. (2005) and Camredon et al. (2007). GECKO-A has been used to predict SOA in a number of studies (e.g., Aumont et al., 2012; Lannuque et al., 2018; McVay et al., 2016), including camphene (Afreh et al., 2020). Details of the camphene mechanism and SOA box modeling were described in Afreh et al. (2020). Briefly, the camphene mechanism includes 1.3×10^6 reactions and 1.8×10^5 oxidation products; vapor pressures of products were calculated based on the Nannoolal method (Nannoolal et al., 2008).

~~In this work, the~~The initial conditions for the GECKO-A simulations were chosen to best represent idealized~~not exactly same to the chamber experimental conditions.~~; that is, initial camphene and NO_x mixing ratios were fixed based on target values for the chamber experiments and not modified to reflect actual values used.The GECKO-A simulations were performed for ~~at~~ a predefined set of conditions, prior to the chamber ~~earlier than the~~ experiments, ~~in which the actual conditions differed from the predefined~~and thus in some cases differ from the experimental conditions. GECKO-A simulations were performed under two NO_x conditions, with 80 ppb of NO_x and without NO_x (Table 1). For both NO_x conditions, the initial hydrocarbon mixing ratios were set at 10, 25, 50, 100, and 150 ppb. All simulations were run under the following initial conditions: 1000 ppb of H_2O_2, 1 µg m^{-3} of organic seed with molecular weight of 250 g mol^{-1}, 298 K temperature, 1% relative humidity, and 50° solar zenith angle (required to compute the photolysis frequencies). Simulation results for camphene were compared with chamber data including SOA mass yields, precursor decay rates, and oxidant levels.

3. Experimental and Modeling Results

Table 2 summarizes the measured initial NO/NO_2 mixing ratios, initial camphene concentration ([HC]$_0$), reacted camphene concentration (Δ[HC]), SOA mass (M_o) formed, particle density, final peak particle diameter (d_p), photochemical aging time, irradiation time, and SOA mass yield (SOA mass formed, M_o/hydrocarbon reacted, ΔHC) for all 13 experiments. Except for Fig. 4, in which SOA mass yields are shown as a function of photochemical age,

all SOA mass yields refer to the mass at the end of the experiments (~6 hours). Measured and predicted gas-phase

220   species are presented in Sect. 3.1; SOA mass and yields are presented in Sect. 3.2. The predicted fate of RO_2 in the

context of initial HC to initial NO_x mixing ratio ($[HC]_0/[NO_x]_0$) is presented in Sect. 3.3.

Table 2. Chamber SOA data, WO indicates experiments without added NO_x and W with added NO_x.

Expt.	Initial NO/NO_2	$[HC]_0$	$\Delta[HC]$	M_o	PM den.	[**]Peak d_p	Irradiation time	Photochemical aging time	SOA mass yYield
	ppb	µg m⁻³	µg m⁻³	µg m⁻³	g cm⁻³	nm	hour	hour	
WO1	0/0	41	41	6.1	1.42	126	4.9	16.1	0.15
WO2	0/0	49	49	3.7	1.42	125	5.0	16.7	0.08
WO3	0/0	155	153	42.0	[*]1.36	214	6.1	17.7	0.27
WO4	0/0	313	305	84.4	[*]1.34	270	6.7	15.8	0.28
WO5	0/0	663	597	158.6	1.30	286	6.7	9.5	0.27
WO6	0/0	1230	844	162.4	[*]1.31	492	6.1	5.0	0.19
W1	86/2	40	40	14.6	1.46	120	5.1	50.6	0.36
W2	114/24	140	140	46.1	1.47	188	5.2	40.6	0.33
W3	51/11	177	177	112.3	[*]1.44	185	6.0	42.0	0.64
W4	5/2	238	237	96.0	1.35	290	5.9	16.1	0.41
W5	45/49	334	334	199.5	[*]1.44	430	5.8	33.6	0.60
W6	42/56	724	724	428.8	[*]1.42	665	5.8	12.7	0.59
W7	45/15	956	950	494.3	[*]1.39	800	6.4	8.75	0.52

[*] Estimated using best fit line shown in Fig. S6.

225 [**] Peak d_p refers to the diameter of particles at the peak of the size distribution plot at the end of the experiment. The uncertainty of peak d_p values is less than 5%.

3.1 Gas-Phase Reactivity

Figure 1-2 shows measured and predicted camphene consumption for the 13 photooxidation experiments, and the calculated time-dependent β values (ratio of $RO_2 + NO$ to the sum of $RO_2 + NO$ and $RO_2 + HO_2$) (Henze et al., 2008;

230 Pye et al., 2010) based on SAPRC predictions for each experimental condition. Additional comparisons of measured and predicted gas-phase species are shown in Fig. S1 and Fig. S2. Higher camphene decay rates and higher OH levels (0.15–0.88 ppt with added NO_x; 0.05–0.29 ppt without added NO_x) were observed and predicted for experiments with added NO_x than without; likely due to the fast recycling of OH when NO_x was present (Fig. 1-2). For all experiments, the β values changed as a function of time due to changing chemical conditions. Note that due to off-gassing of NO_x

235 from the Teflon reactor (Carter et al., 2005), β values simulated here were larger than 0 even for experiments without added NO_x. Experiments with added NO_x have β values from 0.12–1, while experiments without added NO_x have values < 0.12. For all parameters (camphene consumption, NO_x decay, O_3 formation, and OH levels), the SAPRC simulation results were generally in good agreement with the experimental data. The exception to the generally good agreement was O_3 predictions in experiments without added NO_x, which have a relatively strong dependence on the

240 HONO off-gassing rate. The quantity $\Delta([O_3]-[NO])$ has been used to evaluate the rate of NO oxidation by RO_2 for VOC-NO_x systems in SAPRC mechanism development (Carter and Lurmann, 1990; Carter, 1999; Carter, 2009; Carter, 2020). Figure S2 shows the comparison of the $\Delta([O_3]-[NO])$ values between chamber measurements and SAPRC simulations for experiments with added NO_x. The SAPRC box model captures the rates of RO_2+NO well, and supports

the use of the SAPRC model to interpret chamber observations especially in the presence of NO_x. Unfortunately, it is hard to quantify how well constrained the other RO_2 reaction rates and product yields are without corresponding measurements, which are not available. In this case, the SAPRC model was largely used to probe the mechanism (diagnostic) and not to predict yields (prognostic). This consistency between experimental data and SAPRC simulations supports the use of the MechGen generated gas phase camphene mechanisms and SAPRC box model results to interpret chamber observations.
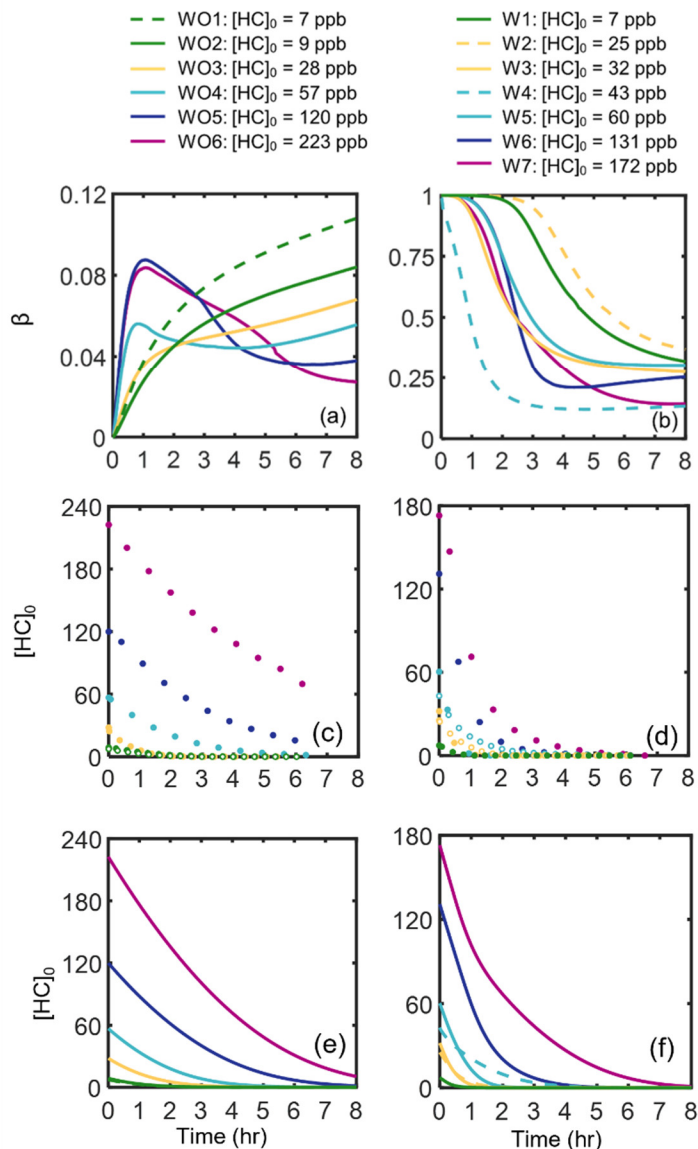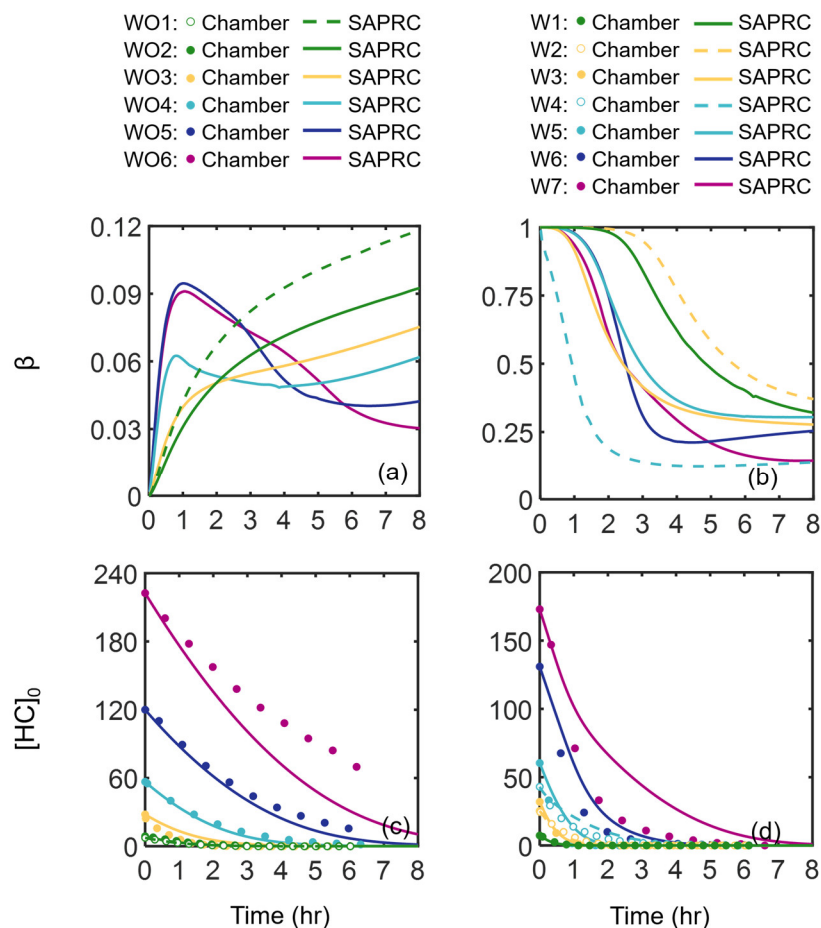
Figure ~~1~~2. SAPRC predicted *β* values: (a) without added NO$_x$, and (b) with added NO$_x$. Measured (circles) and predicted (lines) camphene consumption as a function of irradiation time: (c) without added NO$_x$, and (d) with added NO$_x$. ~~SAPRC predicted camphene consumption: (e) without added NO$_x$, and (f) with added NO$_x$.~~ The hollow makers used in (c) and (d) are equivalent to dashed lines defined in the legends.

255

3.2 SOA Mass and Yield

Measured SOA mass yields ~~(SOA mass formed, *M*$_o$/hydrocarbon reacted, ΔHC)~~ are shown in Fig. ~~2~~3 as a function of SOA mass (*M*$_o$) for experiments with (~~solid~~ squares) and without (~~solid~~ circles) added NO$_x$. ~~The~~The SOA mass

260 yields were much higher in experiments with added NO$_x$ (0.33–0.64) than experiments without added NO$_x$ (0.08–0.28). The observed trends in SOA mass yields were unexpected based on prior chamber studies of SOA formation from monoterpenes, such as OH oxidation studies of α- and β-pinene, in which SOA mass yields were reported to be suppressed under high-NO$_x$ conditions (Eddingsaas et al., 2012; Pullinen et al., 2020; Sarrafzadeh et al., 2016).
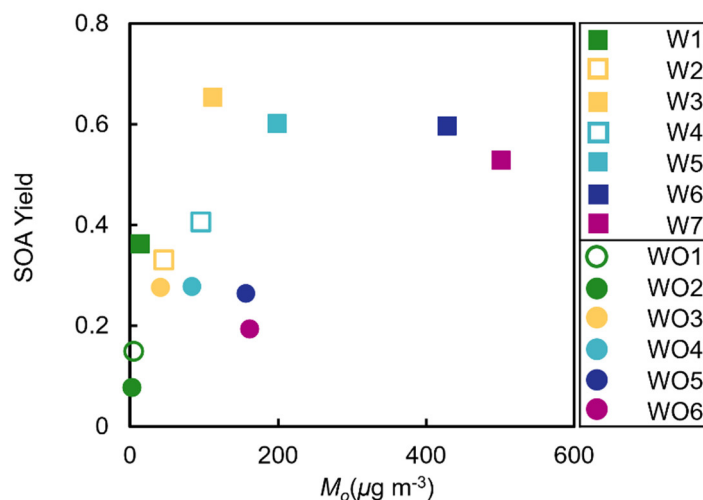
Figure 2̶3. Measured camphene SOA mass yields as a function of SOA mass (M_o). Squares indicate experiments with (W) and circles without (WO) added NO$_x$. Initial HC mixing ratios are differentiated by color; open symbols are used to indicate replicate initial HC mixing ratios.

Figure 2̶ 3 shows another unexpected observation: the SOA mass yields decreased at high SOA mass under both NO$_x$ conditions, which was captured in the measurements and also in the GECKO-A model simulations (see Sect. 5). In the presence of NO$_x$, the observed SOA mass yields increased with M_o for $M_o \leq 112$ µg m^{-3}, plateaued between 112 µg m^{-3} < $M_o \leq 429$ µg m^{-3}, and then decreased for $M_o > 429$ µg m^{-3}. Without NO$_x$, the observed SOA mass yields increased for $M_o \leq 42$ µg m^{-3}, plateaued between 42 µg m^{-3} < $M_o \leq 159$ µg m^{-3}, and then decreased for $M_o > 159$ µg m^{-3}. These unexpected trends in SOA mass yields were further investigated and largely explained by the RO$_2$ fate based on t̶h̶e̶ box model simulations (see Sect. 4 & 5).

The varying [OH] levels in the chamber experiments led to a wide range of photochemical aging times, from hours to days. The irradiation time was converted to equivalent photochemical aging time in the ambient atmosphere using equation (1) (Aumont et al., 2012):

$$\tau = \frac{1}{[OH]_{atm}} \int\limits_{0}^{t} [OH]_{sim} dt \tag{1}$$

where [OH]$_{atm}$ was assumed to be 2×10^6 molecule cm^{-3}. Figure 3̶ 4 shows the measured SOA mass yields as a function of photochemical aging time calculated using OH values predicted by SAPRC ([OH]$_{sim}$). ̶T̶h̶e̶ ̶S̶O̶A̶ ̶y̶i̶e̶l̶d̶s̶ ̶i̶n̶ ̶e̶x̶p̶e̶r̶i̶m̶e̶n̶t̶s̶ ̶w̶i̶t̶h̶ ̶a̶n̶d̶ ̶w̶i̶t̶h̶o̶u̶t̶ ̶a̶d̶d̶e̶d̶ ̶N̶O̶x̶ ̶a̶r̶e̶ ̶d̶e̶p̶e̶n̶d̶e̶n̶t̶ ̶o̶n̶ ̶O̶H̶ ̶l̶e̶v̶e̶l̶s̶ ̶a̶n̶d̶ ̶t̶h̶u̶s̶ ̶p̶h̶o̶t̶o̶c̶h̶e̶m̶i̶c̶a̶l̶ ̶a̶g̶i̶n̶g̶ ̶t̶i̶m̶e̶.̶ ̶H̶i̶g̶h̶e̶r̶ ̶[̶H̶C̶]̶0̶ ̶g̶e̶n̶e̶r̶a̶l̶l̶y̶ ̶l̶e̶d̶ ̶t̶o̶ ̶s̶t̶e̶e̶p̶e̶r̶ ̶i̶n̶c̶r̶e̶a̶s̶e̶s̶ ̶i̶n̶ ̶S̶O̶A̶ ̶y̶i̶e̶l̶d̶ ̶a̶s̶ ̶a̶ ̶f̶u̶n̶c̶t̶i̶o̶n̶ ̶o̶f̶ ̶a̶g̶i̶n̶g̶ ̶t̶i̶m̶e̶.̶ ̶E̶x̶p̶e̶r̶i̶m̶e̶n̶t̶s̶ ̶w̶i̶t̶h̶ ̶a̶d̶d̶e̶d̶ ̶N̶O̶x̶ ̶g̶e̶n̶e̶r̶a̶l̶l̶y̶ ̶h̶a̶d̶ ̶l̶o̶n̶g̶e̶r̶ ̶p̶h̶o̶t̶o̶c̶h̶e̶m̶i̶c̶a̶l̶ ̶a̶g̶i̶n̶g̶ ̶t̶i̶m̶e̶s̶ ̶t̶h̶a̶n̶ ̶e̶x̶p̶e̶r̶i̶m̶e̶n̶t̶s̶ ̶w̶i̶t̶h̶o̶u̶t̶ ̶a̶d̶d̶e̶d̶ ̶N̶O̶x̶.̶ ̶I̶n̶ ̶a̶d̶d̶i̶t̶i̶o̶n̶,̶ ̶i̶n̶ ̶e̶x̶p̶e̶r̶i̶m̶e̶n̶t̶s̶ ̶w̶i̶t̶h̶ ̶a̶d̶d̶e̶d̶ ̶N̶O̶x̶,̶ ̶t̶h̶e̶ ̶y̶i̶e̶l̶d̶ ̶c̶u̶r̶v̶e̶s̶ ̶m̶o̶s̶t̶l̶y̶ ̶p̶l̶a̶t̶e̶a̶u̶e̶d̶ ̶b̶y̶ ̶t̶h̶e̶ ̶e̶n̶d̶ ̶o̶f̶ ̶t̶h̶e̶ ̶e̶x̶p̶e̶r̶i̶m̶e̶n̶t̶;̶ ̶h̶o̶w̶e̶v̶e̶r̶,̶ ̶i̶n̶ ̶m̶o̶s̶t̶ ̶o̶f̶ ̶t̶h̶e̶ ̶e̶x̶p̶e̶r̶i̶m̶e̶n̶t̶s̶ ̶w̶i̶t̶h̶o̶u̶t̶ ̶a̶d̶d̶e̶d̶ ̶N̶O̶x̶,̶ ̶t̶h̶e̶ ̶y̶i̶e̶l̶d̶ ̶c̶u̶r̶v̶e̶s̶ ̶w̶e̶r̶e̶ ̶s̶t̶i̶l̶l̶ ̶i̶n̶c̶r̶e̶a̶s̶i̶n̶g̶ ̶a̶t̶ ̶t̶h̶e̶ ̶e̶n̶d̶ ̶o̶f̶ ̶t̶h̶e̶ ̶e̶x̶p̶e̶r̶i̶m̶e̶n̶t̶s̶.̶ The SOA mass yields are dependent on OH levels and thus photochemical aging time. The yield curves for most experiments plateaued or nearly plateaued by the end of the experiment. Higher [HC]$_0$ generally led to steeper increases in SOA mass yield as a function of aging time. Experiments with added NO$_x$ generally had longer photochemical aging times than

experiments without added NO_x; even at the same aging time (Fig. S8), the SOA yields were higher in the with added
NO_x experiments. The higher SOA mass yields in experiments with added NO_x may partially be attributed to the
difference in [OH] levels and extents of aging. Similar NO_x effects have been reported in many previous studies (e.g.,
Ng et al., 2007a; Sarrafzadeh et al., 2016). Sarrafzadeh et al. (2016) proposed that in a study of β-pinene the OH level
was the main factor that accounted for differences in SOA mass yields under varying $[NO_x]_0$. In the camphene
experiments presented herein, except for some of the experiments without added NO_x, the aging effects were
determined to be less important than RO_2 chemistry, since the SOA mass yield curves as a function of photochemical
aging already plateau or nearly plateau by the end of experiments (Fig. 34).
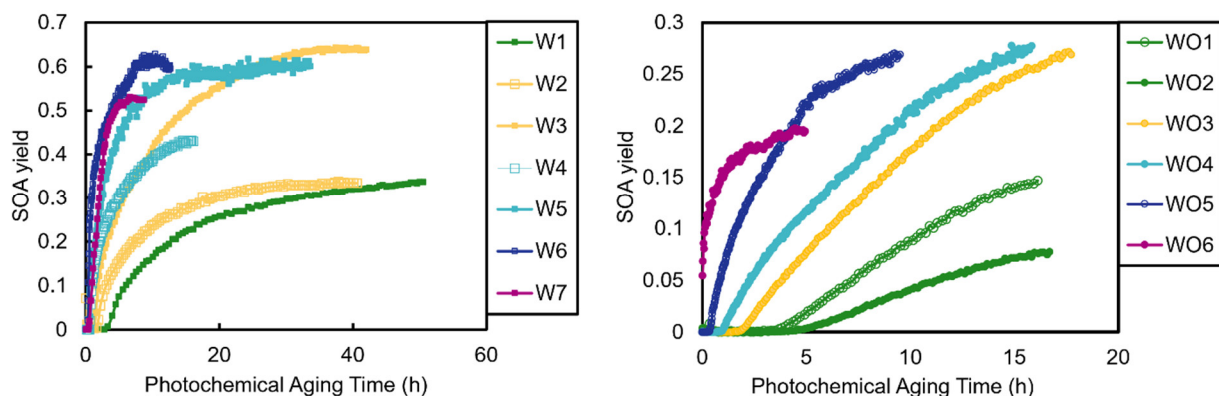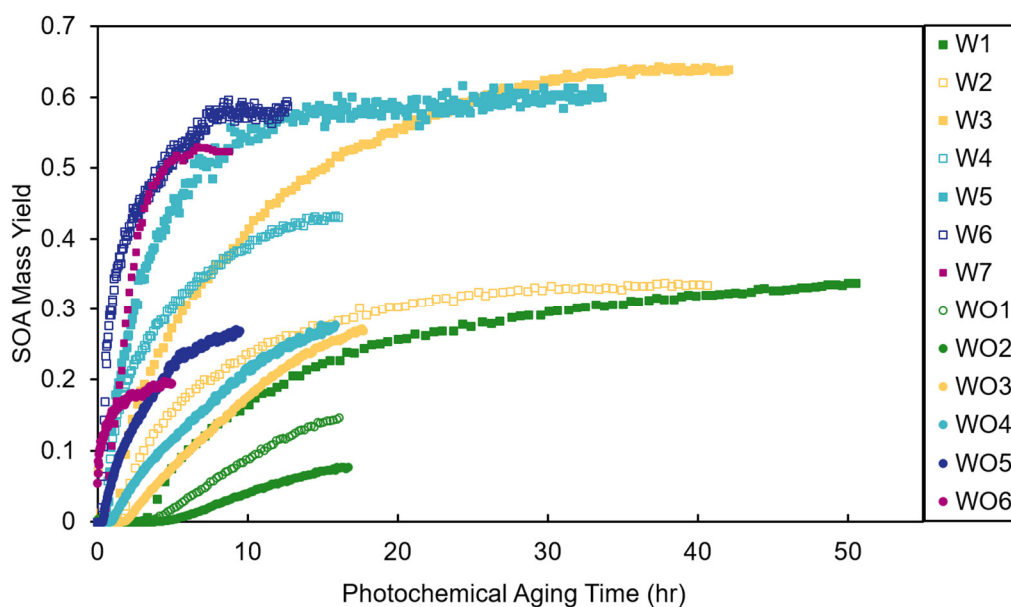
Figure 34. Measured SOA mass yields as a function of photochemical aging time in experiments with added NO_x (asquares),;
and experiments without added NO_x (circlesb).

SOA mass yields were are shown as a function of Δ[HC], $[HC]_0/[NO_x]_0$, and photochemical aging time in Fig. 45.
For the experiments without added NO_x, a constant value of 1 ppb was used in the calculations of $[HC]_0/[NO_x]_0$ to
account for NO_x off-gassing from the Teflon reactors. Based on recent characterization experiments, the UCR chamber

has a NO_x off-gassing rate of 2.8 ppt/min in the form of HONO; the camphene experiments lasted for ~300 to 360

305 mins. Over low $\Delta[HC]$ ranges, when $\Delta[HC]$ increases, SOA mass yield increases as well. When $\Delta[HC]$ is larger than

approximately 200 ug m^{-3}, this correlation becomes less apparent, due to the high sensitivity of SOA formation on

$[HC]_0/[NO_x]_0$ over the range of $\Delta[HC]$ sampled. At a given $\Delta[HC]$ level, a relatively smaller $[HC]_0/[NO_x]_0$ (when it

was within 0.5–200) would lead to a higher SOA mass yield (decreasing $[HC]_0/[NO_x]_0$ by approximately 100 times

may double the SOA mass yield). The chamber data presented here exhibit a general trend that, under the regular

310 regime (distinguished from the extreme $[NO_x]$ regime), higher SOA mass yields are observed from camphene

oxidation at higher $\Delta[HC]$ and smaller $[HC]_0/[NO_x]_0$. This is different from studies of α-pinene, in which smaller

$[HC]_0/[NO_x]_0$ generally led to ~~smaller~~ lower SOA mass yield (Eddingsaas et al., 2012).
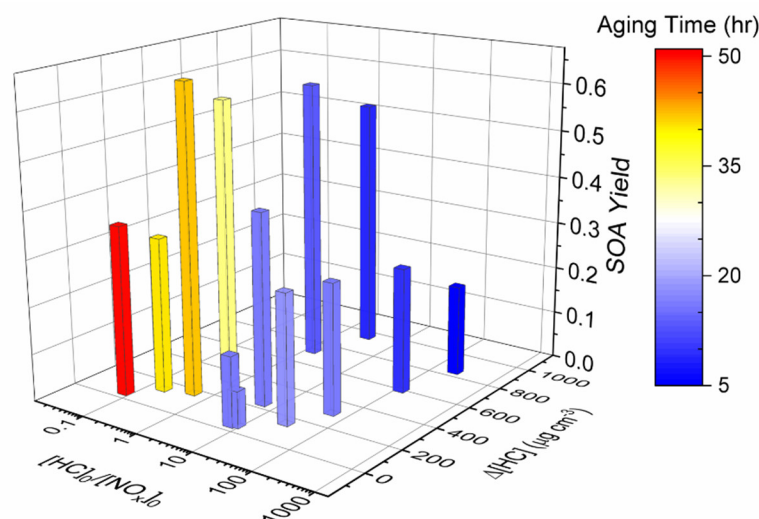
Figure 4~~5~~. SOA mass yields dependence on $[HC]_0/[NO_x]_0$, $\Delta[HC]$, and photochemical aging time.

315 **3.3 $[HC]_0/[NO_x]_0$ and the Fate of Peroxy Radicals**

Table S1 shows the experimental $[HC]_0/[NO_x]_0$ and the SAPRC predicted fate of total RO_2 (calculated as the

summation of RO_2 radicals that undergo bimolecular reactions~~the summation of all the RO_2 radicals formed from~~

~~camphene and camphene products~~) for all the chamber runs.~~-~~ In Fig. 5~~6~~, the fate of total RO_2 is shown as a function

of $[HC]_0/[NO_x]_0$. The majority of RO_2 was predicted to undergo bimolecular reactions with HO_2 or NO across the

320 range of $[HC]_0/[NO_x]_0$ values sampled. At $[HC]_0/[NO_x]_0 < 6$, $> 50\%$ of the RO_2 was predicted to react with NO; and

at $[HC]_0/[NO_x]_0 > 10$, $> 50\%$ of the RO_2 was predicted to react with HO_2. A roughly 50:50 branching of RO_2 between

NO and HO_2 was reached when $[HC]_0/[NO_x]_0$ was 6:1, which is close to the ratio that was suggested in Presto et al.

(2005). When $[HC]_0/[NO_x]_0$ increased over 50, the total fraction of bimolecular RO_2 + RO_2 ~~and unimolecular RO_2~~

~~reactions~~ increased from 0 to 3~~4~~0%. In addition, the normalized total RO_2 concentration (~~accumulated~~ total

325 $[RO_2]/[HC]_0$, ppbv/ppbv) increased as $[HC]_0/[NO_x]_0$ decreased (~~Fig. 4 and~~ Fig. 6~~7~~), suggesting ~~higher~~more

oxygenated -RO_2s ~~iterations~~ were ~~achieved~~formed by NO pathway than others, which is consistent with the formation

of HOMs with added NO_x. There is a general trend of increasing SOA mass yield with decreasing $[HC]_0/[NO_x]_0$ (Fig.

4~~5~~ and Fig. 6~~7~~), with the exception of four outliers (W1, W2, WO1, and WO2) that have relatively low SOA mass

yields. Experiments WO1, WO2, W1 had the lowest Δ[HC] (49, 41, and 40 μg/m^3, respectively, Table 2), indicating

330   the SOA mass yields were influenced by Δ[HC] as well as RO$_2$ chemistry. The connections between the fate of RO$_2$
and observed SOA mass yields are further discussed in Sect. 4. Though vapor wall loss has been found to be negligible
in previous UCR chamber experiments, such experiments were typically conducted at higher [HC]$_0$. Thus, it is
acknowledged that vapor wall loss could affect the measured SOA yields, particularly for experiments W1-2 and
WO1-2 with low [HC]$_0$ (or M_o). A vapor wall loss correction for those experiments would increase the measured SOA,

335   but would not affect the following discussion or conclusions regarding the role of RO$_2$ chemistry.
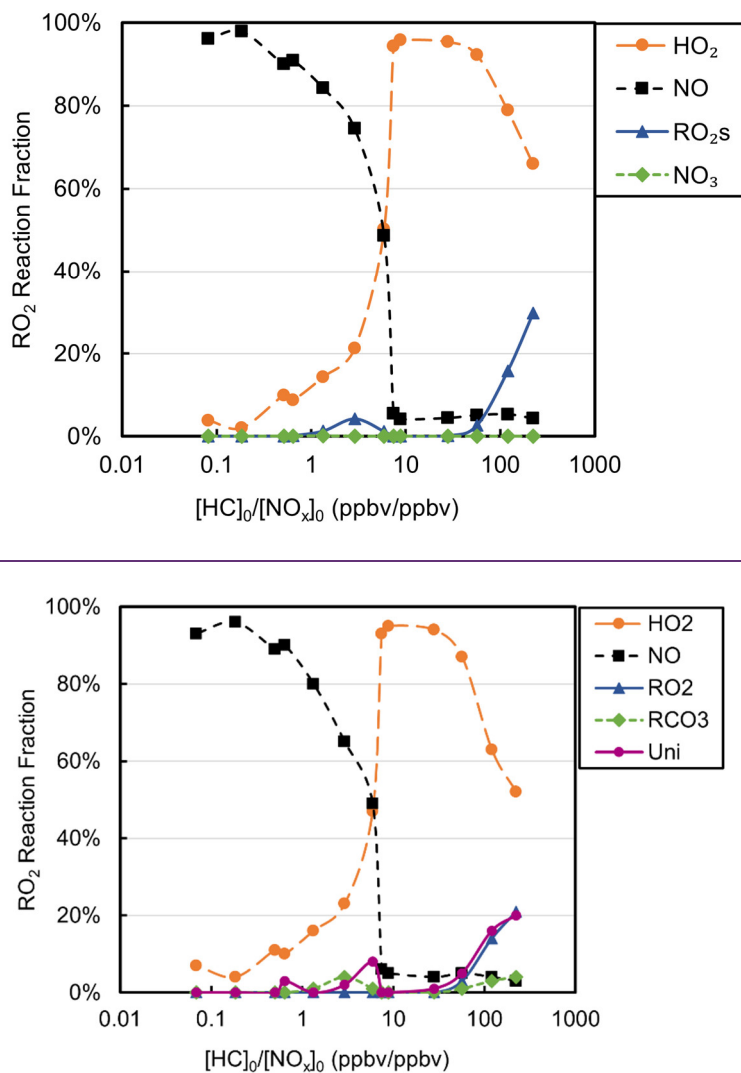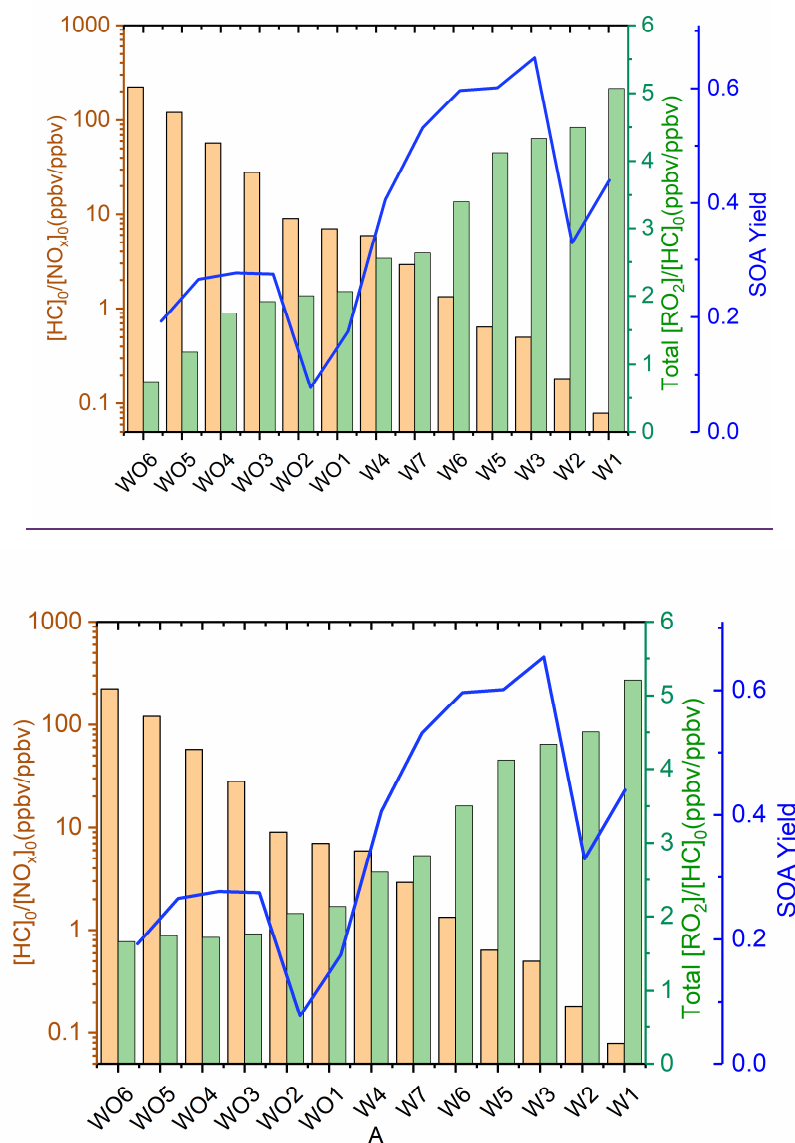

Figure 5̶6̶. – Fractions of total RO$_2$ reactions of each type as a function of [HC]$_0$/[NO$_x$]$_0$ based on Table S1.

Figure 6̶7. Relationship between a̶c̶c̶u̶m̶u̶l̶a̶t̶e̶d̶ total [RO₂]/[HC]₀, [HC]₀/[NOₓ]₀, and SOA mass yields.

By assuming the gas-phase chemistry and product distribution were similar when $RO_2 + NO$ accounted for more than 80% of the total RO_2 consumption and when $RO_2 + HO_2$ accounted for more than 80% of the total RO_2 consumption,- experiments with (W1–3, 5–6) -and without (WO1–4) added NO_x were grouped and used to derive SOA parameters using the two-product (Odum et al., 1996) and VBS approaches (Donahue et al., 2006; Donahue et al., 2009). The resultant parameters are shown in Table 3 (two-product) and Table 4 (VBS).

Table 3. Two-Product Model SOA parameters.

	α_1	$\log_{10} C^*_1$	α_2	$\log_{10} C^*_2$
Without NO_x	0.0017	1.08	0.3139	0.92
With NO_x	0.4484	1.77	0.2398	-2.94

Table 4. VBS Model SOA parameters.

~~log~~$_{10}$C*	$^{\dagger}\alpha_{wo}$	$^{\dagger}\alpha_w$
0.1	0.0001	0.2657
~~0~~1	0.0152	0.0008
10	0.3069	0.0357
100	0.0001	0.4222
1000	0.0003	0.0000

† wo refers to without added NO_x; w refers to with added NO_x.

4 Discussion

The reaction rate constant of camphene with O_3 is relatively low compared to OH, and thus it is expected that OH is the dominant oxidant in the photooxidation of camphene under chamber conditions,~~;~~ especially with the high initial H_2O_2 (~1 ppm) concentrations. This is supported by SAPRC simulation results (see Fig. S3 in SI), in which ~~SAPRC predicted that~~ O_3 accounts for 0–3% and NO_3 for 0–16% of camphene oxidation, demonstrating the important role of OH oxidation in these studies.

4.1 Camphene + OH Gas-phase Mechanism

Figure ~~7~~8 shows the MechGen predicted reactions and products of OH-initiated oxidation of camphene in the presence of NO_x through one major pathway, which had a yield of 0.83 (a more detailed reaction mechanism schematic is presented in Fig. S4). The reaction starts with OH addition to the CH_2=(C) position to form a ring-retaining alkyl radical, which further reacts with O_2 to form the camphene peroxy radical, RO_2-a. RO_2-a can react with oxidants (NO, NO_3, HO_2, and/or other RO_2) to create an alkoxy radical, RO-a, with NO to NO_2 conversion; or form stable products such as organic nitrate (NO3CAMP1), hydroperoxide (HO2CAMP1), and ~~phenolic~~ alcohol (RO2CAMP1) compounds. The cyclic alkoxy radical RO-a can undergo prompt beta (β)-scission ring-opening reaction, and then O_2 addition to form another peroxy radical, RO_2-b. In the presence of NO_x, rapid β-scission decomposition, or ring-opening reactions of the camphene alkoxy radicals (RO-b and RO-c) occur through the RO_2 + NO pathway, leading to the generation of the peroxy radical RO_2-d with lower carbon number and higher O:C ratio (increases from 0.30 for RO_2-a to 0.71 for RO_2-d).
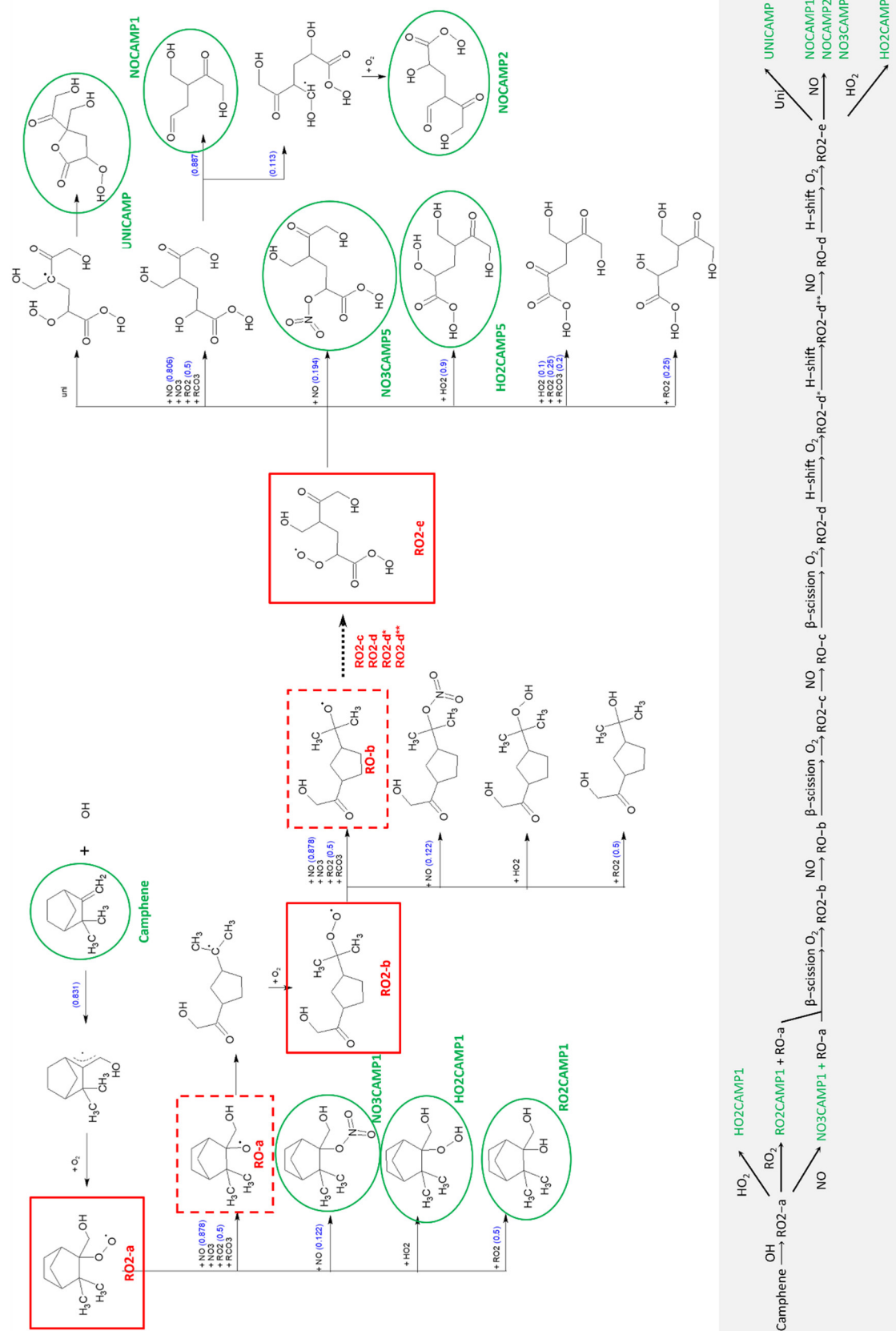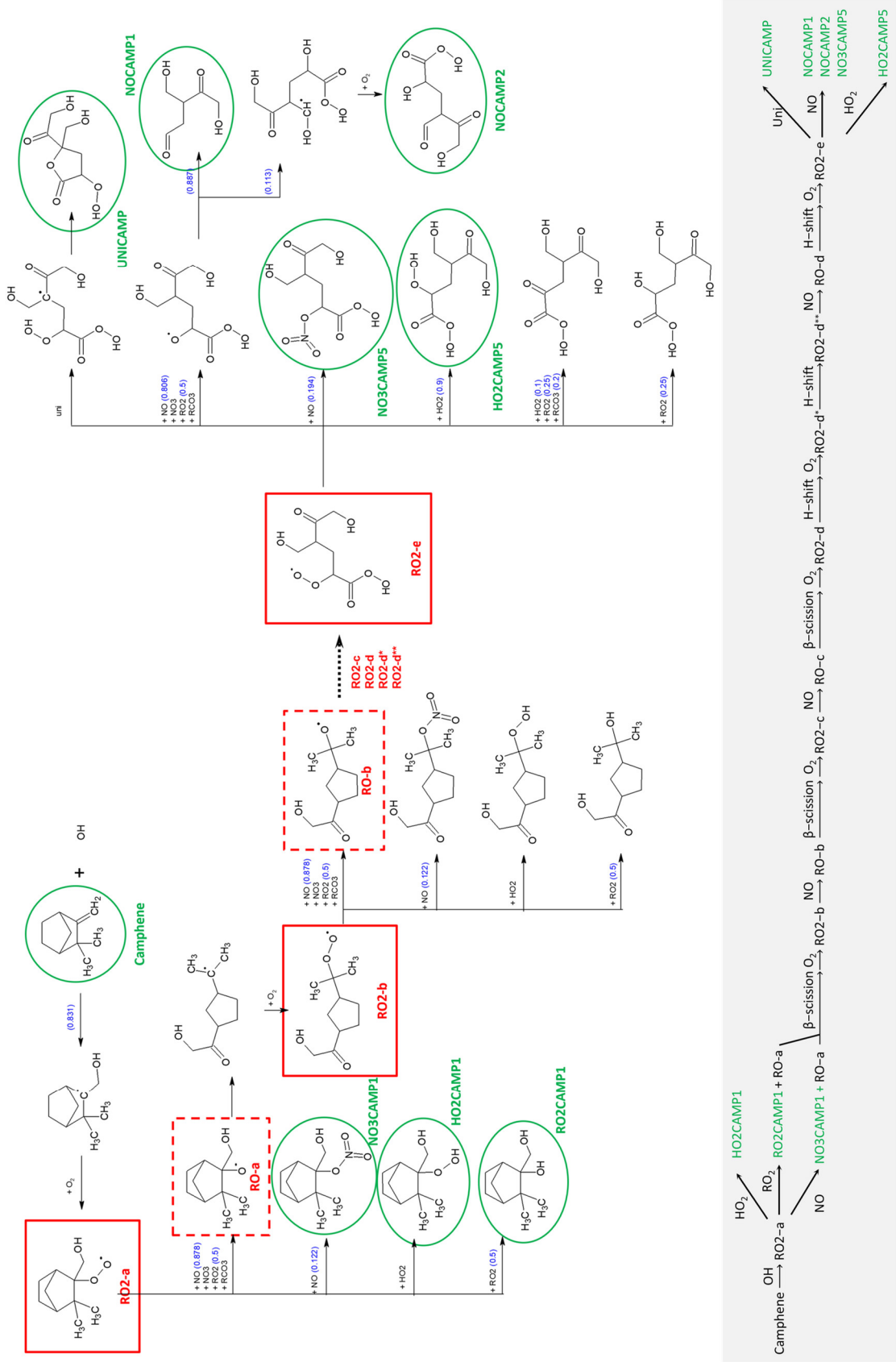
Figure 78. Schematic of the OH-initiated oxidation of camphene mechanism in SAPRC at 298 K and atmospheric pressure in the presence of NO$_x$. Check Fig. S4 for more details.

370   MechGen predicted that RO$_2$-d could undergo 1,5 H-shift isomerization nearly instantaneously, even in the presence of ~ 100 ppb NO$_x$. Subsequent rapid addition of O$_2$ can form a new peroxy radical RO$_2$-d* which ~~could~~ can undergo 1,7 H-shift isomerization and form the peroxy radical RO$_2$-d**. RO$_2$-d** can participate in termination reactions with NO and HO$_2$ to form organic nitrate (NO3CAMP4) and hydroperoxide (HO2CAMP4) products, which are known as highly oxygenated organic molecules (HOMs). In the presence of NO$_x$, RO$_2$-d** can also react with NO

375   to form the alkoxy radical RO-d that can undergo 1,4 H-shift isomerization and then O$_2$ addition to form the new peroxy radical RO$_2$-e which will also lead to the formation of HOMs such as NO3CAMP5, HO2CAMP5, and UNICAMP. A recent SOA study by Mehra et al. (2020) demonstrated the formation of HOMs in camphene chamber experiments under both low NO$_x$ (30 ppb camphene, ~ 0 ppb NO$_x$) and medium NO$_x$ (30 ppb camphene, 2.2 ppb NO, 58.4 ppb NO$_2$) conditions. Based on their observations and analysis, the average molecular formula of the camphene

380   SOA was C$_{7.26}$H$_{9.85}$O$_{4.03}$ for low NO$_x$ and C$_{6.63}$H$_{9.7}$N$_{0.12}$O$_{4.21}$ for the medium NO$_x$ conditions, which also suggest~~ed~~ the occurrence of ring-opening and decomposition reactions during camphene photooxidation, as predicted by MechGen.

4.2 The Formation of HOMs and Influence on SOA <u>Mass</u> Yields

Table 5. Log$_{10}$ C* value for selected 1st generation <u>of stable end products formed from camphene reactions with OH</u>~~products~~.

Species	Atom				O:C	log$_{10}$ C*	Species	Atom				O:C	log$_{10}$ C*
	C	H	O	N				C	H	O	N		
HO2CAMP1	10	18	3	0	0.30	2.5	NO3CAMP1	10	17	4	1	0.40	3.5
HO2CAMP2	10	18	4	0	0.40	1.7	NO3CAMP2	10	17	5	1	0.50	2.6
HO2CAMP3	7	12	4	0	0.57	2.5	NO3CAMP3	7	11	5	1	0.71	3.5
HO2CAMP4	7	12	7	0	1.00	-1.3	NO3CAMP4	7	11	8	1	1.14	-0.1
HO2CAMP5	7	12	8	0	1.14	-4.3	NO3CAMP5	7	11	9	1	1.29	-2.8
RO2CAMP1	10	18	2	0	0.20	3.8	NOCAMP1	6	10	4	0	0.67	2.6
UNICAMP	7	10	7	0	1.00	-3.9	NOCAMP2	7	10	7	0	1.00	-1.1

385

Table 6. Fractions of peroxy radical RO$_2$-a reactions of each type, calculated based on SAPRC simulations.

Expt.	[HC]$_0$ (ppb)	*[HC]$_0$/[NO$_x$]$_0$ (ppbv/ppbv)	SOA Mass Yield	Fraction of RO$_2$-a Reaction				
				NO	HO$_2$	RCO$_3$	RO$_2$	NO$_3$
WO1	7	7	0.15	0.03	0.97	0	0	0
WO2	9	9	0.08	0.02	0.98	0	0	0
WO3	28	28	0.27	0.02	0.97	0	0	0
WO4	57	57	0.28	0.03	0.89	0	0.08	0
WO5	120	120	0.27	0.03	0.64	0.02	0.30	0
WO6	223	223	0.19	0.03	0.54	0.02	0.41	0
W1	7	0.08	0.36	1.00	0	0	0	0
W2	25	0.18	0.33	1.00	0	0	0	0
W3	32	0.51	0.64	0.97	0.03	0	0	0
W4	43	5.91	0.41	0.46	0.53	0.01	0	0
W5	60	0.64	0.60	0.97	0.03	0	0	0
W6	131	1.33	0.59	0.88	0.12	0.01	0.01	0
W7	172	2.88	0.52	0.65	0.30	0.03	0.01	0

*The [HC]$_0$/[NO$_x$]$_0$ for WO1–6 experiments were estimated assuming 1 ppb of NO$_x$.

Table 5 lists the log C^* values and O:C ratios for the major camphene products predicted; vapor pressures of products were calculated based on the Nannoolal method (Nannoolal et al., 2008). HOMs have much lower volatilities than the earlier terminal products such as NO3CAMP1, HO2CAMP1, and RO2CAMP1. HOMs formed by autoxidation steps in camphene radical chain reactions are mediated by the H-shift isomerization of RO$_2$-d and RO-d. Table 6 shows the SAPRC predicted fate of RO$_2$-a for all chamber runs; the fate of summed RO$_2$ is shown in Table S1, which includes RO$_2$-a~d and all the RO$_2$ radicals formed from other minor pathways. For the experiments without added NO$_x$ (WO1–6), once the initial peroxy radical RO$_2$-a was formed, a large fraction of RO$_2$-a (0.54-0.98) quickly reacted with HO$_2$ to form the terminal product HO2CAMP1, while only 2–3% of RO$_2$-a reacted through the NO pathway and led to the generation of HOMs. For the experiments with added NO$_x$ (W1–7), much higher RO$_2$-a + NO fractions (0.65–1.00) were predicted by SAPRC. The fates of summed RO$_2$ also suggested that not only RO$_2$-a, but also the other RO$_2$ radical intermediates would tend to favor further reactions through the NO reaction chain to form lower volatility products.

Based on the predicted fate of RO$_2$ in SAPRC simulations, the higher SOA mass yields in experiments with NO$_x$ were due to the formation of HOMs through autoxidation in the presence of NO$_x$. In general, faster RO$_2$ reaction with NO, HO$_2$ or other RO$_2$ limits HOM formation by autoxidation (Bianchi et al., 2019). In previous monoterpene SOA studies, HOM formation was often observed when NO$_x$ was absent or under lower NO$_x$ conditions (Pye et al., 2019; Schervish and Donahue, 2020; Zhao et al., 2018). For example, Zhao et al. (2018) demonstrated that autoxidation for some RO$_2$ is competitive with RO$_2$ + NO at ppb levels of NO for O$_3$-initiated α-pinene oxidation. They also reported that HOM formation decreased as the initial NO concentration increased from 0 ppb to 30 ppb. In the camphene experiments presented herein, the reverse trend was observed (see experiments WO4, W4 and W5 conducted with

~50 ppb camphene at different NO_x levels). This was due to the key RO_2 species, RO_2-d, which was predicted to form only in the presence of NO_x and had a fast enough autoxidation rate constant to effectively compete with bimolecular reactions.

The decreasing SOA mass yields at high $[HC]_0$ and M_o in all experiments (shown in Fig. ~~2~~3) can also be explained by RO_2 chemistry. For experiments with added NO_x, the decreasing SOA mass yield trend was most likely due to the shift of RO_2 reaction pathways from NO to HO_2. The fraction of RO_2-a + NO decreased from 0.97 (W5) to 0.65 (W7) while the fraction of RO_2-a + HO_2 increased from 0.03 (W5) to 0.3 (W7). For the experiments without NO_x, the shift from RO_2 + HO_2 to self- and cross-reactions of RO_2 at high $[HC]_0$ and M_o led to decreasing SOA mass yields. When $[HC]_0$ increased from 57 ppb to 223 ppb, the fractions of RO_2-a + HO_2 decreased from 0.89 (WO4) to 0.54 (WO6) and the fraction of RO_2-a + RO_2 increased by a factor of five, from 0.08 to 0.41. Moreover, this shift from bimolecular reactions with HO_2 to RO_2 as $[HC]_0$ increased also occurred in the context of the total RO_2 (Table S1). Generally, products that were predicted to form from one RO_2 reacting with another RO_2 in the absence of NO_x, had relatively higher volatility than those formed from that RO_2 reacting with HO_2; for example, RO2CAMP1 formed from RO_2-a + RO_2 was more volatile than HO2CAMP1 formed from RO_2-a + HO_2 (Table 5). The increasing fraction of self- and cross-reactions of RO_2 therefore is one likely explanation for the decreasing SOA mass yields at high ΔHC and M_o in the experiments without NO_x.

In experiments W1 and W2, the relatively low SOA mass yields (0.36 and 0.33) can be partially attributed to differences in product distribution. A comparison of the product distributions between W1, W2, W3 and W5 suggested similar yields of NO3CAMP1–5 and NOCAMP1–2, but major differences in yields of UNICAMP and HO2CAMP1– 5 (Fig. S5). Experiments W3 and W5 were selected for comparison because of their closest total RO_2 fractional reaction distribution (approximately 90% RO_2 + NO and 10% RO_2 + HO_2) to W2 (~~96~~98% RO_2 + NO and ~~4~~2% RO_2 + HO_2) and W1 (~~93~~96% RO_2 + NO and ~~7~~4% RO_2 + HO_2) but higher SOA mass yield (0.64 and 0.6). W1 and W2 were predicted to have much smaller SOA mass yield than W3 and W5 in the low volatility products HO2CAMP1–5 (especially product HO2CAMP5, the lowest volatility among all listed products in Table 5, $\log_{10}C^*$ = -4.3) and UNICAMP (the second lowest volatility shown in Table 5, $\log_{10}C^*$ = -3.9), which can contribute to the lower SOA mass yield. Further analysis of W1 and W2 revealed a likely cause for the different yields of HO2CAMP1–5 and UNICAMP. W1 and W2 were predicted to have delayed peaks of [OH] (after 3–4 hours of irradiation) which likely was due to the high NO_x concentrations (Fig. S1b). Correspondingly, the $[HO_2]$ was highly suppressed during the first 2 hours of irradiation. Under high $[NO_x]$, the RO_2-e + HO_2 pathway shown in Fig. ~~7~~8 therefore could be suppressed, resulting in a lower yield of HO2CAMP5. This indicates a second regime may exist at high $[NO_x]$ and significantly lower $[HC]_0/[NO_x]_0$.

5 GECKO-A simulations

5.1 SOA Mass and Yield

The comparison of gas- and particle-phase species between chamber experiments and GECKO-A model simulations are shown in Fig. S1a and Fig. S1b. Without added NO_x, GECKO-A predicts much smaller camphene consumption

rates and no O$_3$ formation ~~of O$_3$~~, while both the chamber data and SAPRC simulations suggest a final O$_3$ mixing ratio

of ~10 ppb (Fig. S1a). This may be due to an underrepresentation of data and relevant pathways for low to no NO$_x$ conditions in the GECKO-A mechanism generation system, and the incomplete treatment of wall effects in the application of the GECKO-A box model. The without added NO$_x$ simulations therefore are not further discussed. With added NO$_x$, GECKO-A shows good agreement with the experimental data and SAPRC simulations in the context of camphene consumption, O$_3$, and OH levels.
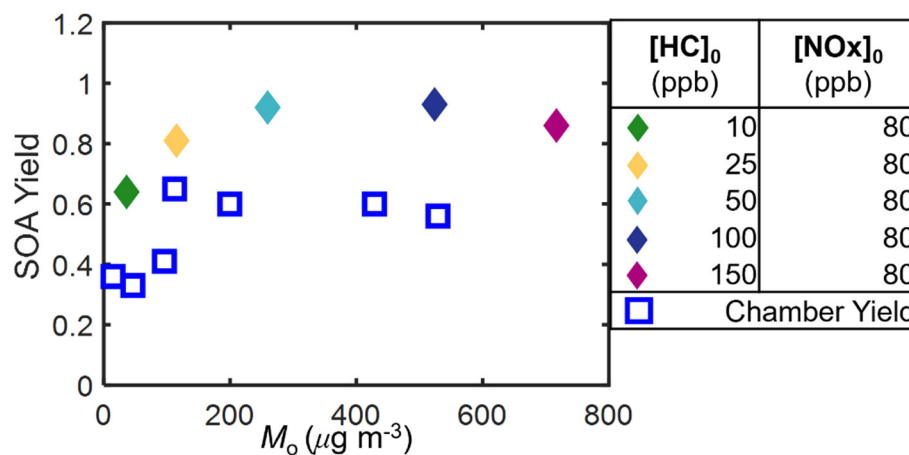
Figure ~~8~~9. Predicted SOA mass yields based on GECKO-A model simulations.

Figure ~~8~~9 shows the predicted SOA mass yields based on GECKO-A. For simulations with added NO$_x$, while the model predicted higher SOA mass yields (0.64–0.93) than were observed (0.33–0.64), the trends in the SOA mass yields were ~~similar~~ consistent between chamber observation and simulations. The simulated SOA mass yield increased with SOA mass for SOA mass < 260 µg m^{-3}, plateaued for SOA mass between 260 and 524 µg m^{-3}, and then decreased for SOA mass > 524 µg m^{-3}.

The ~~decreasing trend in SOA mass yields is represented in the~~ predicted ~~and measured~~ O:C ratio ~~(Fig. 910)~~and ~~a~~The average carbon number (Fig. 10), defined as the ~~used in this study was defined as the~~ mole-weighted averaged carbon number for the main products ~~(~~(~95% by mass), were consistent with the plateauing/decreasing SOA yields at higher [HC]$_0$ (Fig. 9). ~~The~~ The average carbon number was calculated using ~~ion was based on~~ equation (2)~~:, where nC$_i$, M$_{o,i}$, and MW$_i$ are the carbon number, mass, and molecular weight of species i, respectively.~~

$$\text{Average carbon number} = \frac{\sum_i \dfrac{nC_i \times M_{o,i}}{MW_i}}{\sum_i \dfrac{M_{o,i}}{MW_i}} \tag{2}$$

where nC_i, $M_{o,i}$, and MW_i are the carbon number, mass, and molecular weight of species i, respectively. With added NO$_x$, the average carbon number of both the ~~particle and~~ gas and particle phase~~s~~ increase~~ds~~ as [HC]$_0$ increase~~ds~~, while the O:C ratio decreased ~~(Fig. 910)~~. These trends indicate there is a significant fraction of higher volatility compounds formed ~~predicted higher average product carbon numbers suggest that less oxygenated products with smaller O:C (higher volatility) were likely~~ that contribute to SOA at higher [HC]$_0$ (or M_o) resulting in lower~~formed and suppressed the~~ SOA mass yields. ~~This simulation is Higher average product carbon numbers suggest that less oxygenated products with smaller O:C (higher volatility) were formed. The average vapor pressure of products may then increase as [HC]$_0$~~

470 ~~increases, reducing the SOA yield. This is consistent with the chamber results and could contribute to the decreasing SOA~~ mass yield at higher mass loadings (M_o > 524 μg m⁻³) ~~in Fig. 8~~9. In addition, only at the highest two [HC]$_0$ were ~~,~~ ~~the GECKO-A simulation~~ non-negligible fractions of precursor predicted to ~~of 150 ppb HC with NO$_x$ predicts the highest fraction of precursor~~ reacted ~~by~~ with O$_3$ and NO$_3$ (Fig. S7). ~~₃ among all 5 runs~~, suggesting a larger fraction of higher-volatility nitrogen-containing products. More detailed comparisons of GECKO-A simulations with chamber

475 experiments are presented by Afreh et al. (2020) for camphene and McVay et al. (2016) for α-pinene. ~~(Fig. S7). Available AMS data suggest a clear difference in the abundance of nitrogen-containing species between the experiments with and without added NO$_x$. NO$_3$ was predicted to account for an average ~ 14% of total SOA mass in simulations with NO$_x$, and only 1% of total SOA without NO$_x$.~~
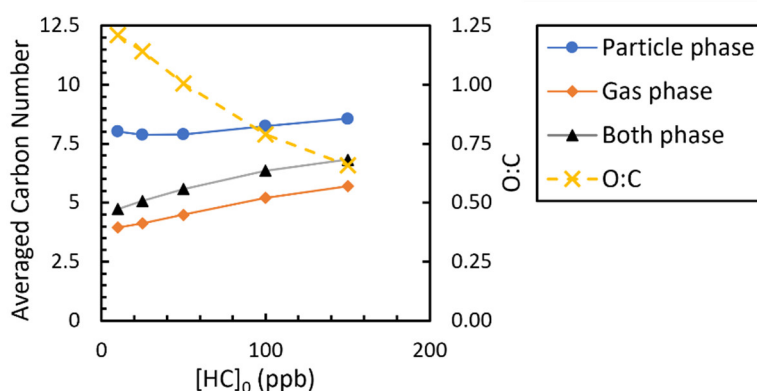
480 **Figure ~~9~~10. ~~GECKO-A p~~Predicted particle O:C and mole-weighted averaged carbon number of products with added NO$_x$. ~~by GECKO-A.~~**

5.2 Particle Density and O:C

Figure 1~~1~~0a shows the GECKO-A predicted O:C ratio and measured O:C ratio as a function of [HC]$_0$/[NO$_x$]$_0$ for all experiments. A good agreement in O:C ratios was observed between the model predictions and chamber data. The

485 O:C ratio decreased from 1.21 to 0.39 as [HC]$_0$/[NO$_x$]$_0$ increased from 0.13 to 223, supporting that more highly oxygenated products were formed at lower [HC]$_0$/[NO$_x$]$_0$.

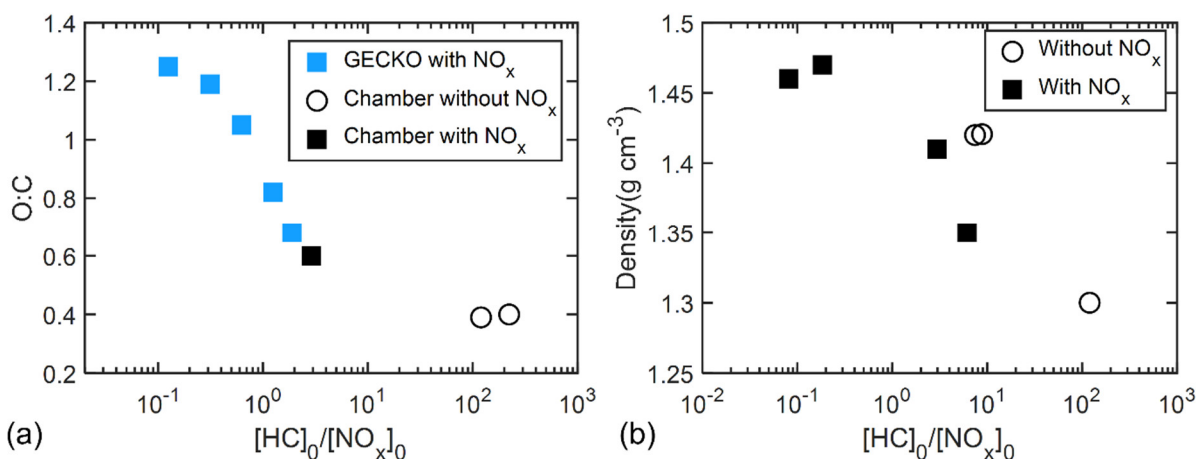**Figure 1011. (a), O:C ratio as a function of [HC]₀/[NOₓ]₀ with AMS data and prediction by GECKO-A simulation. (b), Particle density (directly measured by APM–SMPS) shown as a function of [HC]₀/[NOₓ]₀.**

490　　A negative correlation was also observed between measured particle density and [HC]₀/[NOₓ]₀. The final density of particles decreased from 1.47 g cm⁻³ to 1.30g cm⁻³ as [HC]₀/[NOₓ]₀ increased from 0.08 to 120 (Fig.11~~0~~b). The change in O:C ratio could account for the change in density. O:C and H:C have been used in semi-empirical SOA density parameterizations ~~prediction by semi-empirical equation~~ (Nakao et al., 2013; Kuwata et al., 2012), in which O:C plays a dominant role in determining organic particle density compared to H:C. Consistent with the semi-

495　　empirical formulations, the density of particles formed from oxidation of camphene increased as O:C ~~(ranged from 0.39 to 1.21)~~ increased (from 0.39 to 1.21), while H:C varies over a smaller range (from 1.42 to 1.79). The change in density supports the proposed explanation that more oxygenated products were formed under lower [HC]₀/[NOₓ]₀. The wide range in final density and the correlation with [HC]₀/[NOₓ]₀ shown here ~~is reported for the first time~~has not been previously reported. The SOA mass of each experiment in this study was calculated with its own density of SOA,

500　　instead of applying an averaged density. A list of particle densities used in this study can be found in Table 2.

6 Conclusions

~~Here we present for the~~The first ~~time~~ SOA mass yields from oxidation of camphene based on experiments performed in UCR environmental chamber with varying [NOₓ]₀ are presented herein. Higher SOA mass yields were measured with added NOₓ (0.33–0.64) than without added NOₓ (0.08–0.26) ~~generally~~ at atmospherically relevant OH

505　　concentrations. SOA formation from the oxidation of camphene showed different NOₓ dependence ~~from~~than what has previously been reported for other ~~known~~monoterpenes (e.g., α-pinene, d-limonene) and~~other~~ n-alkanes (carbon≤ 10), in ~~studies of~~which higher SOA mass yields were measured when [NOₓ] was lower (Nøjgaard et al., 2006; Ng et al., 2007b). ~~Here~~For camphene oxidation, higher Δ[HC] and lower [HC]₀/[NOₓ]₀ (within 0.5–200) generally led to higher SOA mass yields. Similar NOₓ dependence ~~of camphene oxidation~~ has been ~~found~~ observed ~~with~~ for two

510　　sesquiterpenes (longifolene and aromadendrene) but was attributed to the production of nonvolatile organic nitrates with no detailed mechanism analysis provided at that time (Ng et al., 2007b).

　　Although [HC]₀/[NOₓ]₀ shows clear correlation with SOA mass yield, ~~it~~this quantity ~~but~~cannot completely represent the underlying RO₂ chemistry~~completely~~. The ~~dependence of SOA mass yields on HC and NOₓ can be explained by~~ RO₂ chemistry and the competition between varying bimolecular RO₂ and unimolecular RO₂ reaction

515　　pathways, ~~generated~~explored using SAPRC MechGen, can be used to explain the dependence of SOA mass yields on HC and NOₓ. The RO₂ + NO pathway favored in experiments with added NOₓ ~~led to the highest production of RO₂ and~~formed HOMs ~~products~~with much lower volatilities than products formed ~~in~~rom other pathways. In addition to the regular regime introduced above, ~~our study~~the results suggested an extreme regime where significantly high [NOₓ] may suppress~~the~~ SOA mass yield. High NOₓ concentration may suppress the HO₂ concentration at the beginning of

520　　the reactions, causing ~~the~~a subsequent reduction in yield of low volatility products such as UNICAMP and HO2CAMP5. This indicates that if the reactions happened under NOₓ-rich environment with extremely high ratios of NO to HO₂ (NO/HO₂~~NO~~), the SOA mass yield from oxidation of camphene ~~could possibly~~might be significantly suppressed. As demonstrated here, ~~S~~simulations with chemically detailed box models such as SAPRC are useful for

~~recommended in~~ identifying SOA formation regimes. ~~Constant β values controls are preferred to be applied in future SOA formation study of monoterpenes to achieve stable NO/HO$_2$/NO.~~

Overall, SOA formation from oxidation of camphene may be ~~potentially~~ larger in polluted environments (e.g., urban environments) than NO$_x$-free environments. This reveals a possible underestimation of SOA formed from oxidation of camphene and ~~possibly~~ potentially other ~~B~~VOCs that are assumed to have lower SOA mass yields at higher NO$_x$ levels~~in current models by assuming similar SOA mass yield dependence~~. Further ~~C~~chamber and modeling studies of other understudied ~~B~~VOCs will be important for identifying other systems in which moderate NO$_x$ levels can promote HOM formation. ~~are therefore important to evaluate and improve model predictions.~~

Data Availability

The experimental and modeling data is available upon request from the corresponding authors. ~~The modeling data used in this paper can be downloaded online: https://github.com/jia-jiang/SAPRC_Camphene.~~

Supplement

The supplement related to this article is available and can be download from~~online at:~~ ACP assigned link.

Author Contributions

QL and JJ contributed equally to the study and share the first authorship. QL performed chamber experiments, data analysis and led the first draft of the manuscript. JJ derived and implemented the camphene mechanism in SAPRC, conducted SAPRC model simulations and led discussions on the chemistry of camphene SOA formation. IA~~S~~ carried out GECKO-A model simulations. QL and JJ interpreted the results and wrote the manuscript with IA~~S~~. QL, JJ, KB and DC finalized the final manuscript. All the listed authors contributed to the revisions of the manuscript. The project was supervised by KB and DC.

Competing Interests

The authors declare that they have no conflict of interest.

Acknowledgements

Reference

560 Afreh, I. K., Aumont, B., Camredon, M., and Barsanti, K. C.: Using GECKO-A to derive mechanistic understanding of SOA formation from the ubiquitous but understudied camphene, Atmos. Chem. Phys. Discuss., https://doi.org/10.5194/acp-2020-829, 2020.

Akagi, S. K., Yokelson, R. J., Burling, I. R., Meinardi, S., Simpson, I., Blake, D. R., McMeeking, G. R., Sullivan, A., Lee, T., Kreidenweis, S., Urbanski, S., Reardon, J., Griffith, D. W. T., Johnson, T. J., and Weise, D. R.:
565 Measurements of reactive trace gases and variable O3 formation rates in some South Carolina biomass burning plumes, Atmos. Chem. Phys., https://doi.org/10.5194/acp-13-1141-2013, 2013.

Atkinson, R. and Arey, J.: Gas-phase tropospheric chemistry of biogenic volatile organic compounds: A review, Atmos. Environ., 37, 197–219, https://doi.org/10.1016/S1352-2310(03)00391-1, 2003.

Atkinson, R., Aschmann, S. M., and Arey, J.: Rate constants for the gas-phase reactions of OH and NO3 radicals and
570 O3 with sabinene and camphene at 296±2 K, Atmos. Environ. Part A, Gen. Top., https://doi.org/10.1016/0960-1686(90)90144-C, 1990.

Aumont, B., Szopa, S., and Madronich, S.: Modelling the evolution of organic carbon during its gas-phase tropospheric oxidation: Development of an explicit model based on a self generating approach, Atmos. Chem. Phys., https://doi.org/10.5194/acp-5-2497-2005, 2005.

575 Aumont, B., Valorso, R., Mouchel-Vallon, C., Camredon, M., Lee-Taylor, J., and Madronich, S.: Modeling SOA formation from the oxidation of intermediate volatility n-alkanes, Atmos. Chem. Phys., 12, 7577–7589, https://doi.org/10.5194/acp-12-7577-2012, 2012.

Baruah, S. D., Gour, N. K., Sarma, P. J., and Deka, R. C.: OH-initiated mechanistic pathways and kinetics of camphene and fate of product radical: a DFT approach, Environ. Sci. Pollut. Res., https://doi.org/10.1007/s11356-017-0646-
580 2, 2018.

Benelli, G., Govindarajan, M., Rajeswary, M., Vaseeharan, B., Alyahya, S. A., Alharbi, N. S., Kadaikunnan, S., Khaled, J. M., and Maggi, F.: Insecticidal activity of camphene, zerumbone and α-humulene from Cheilocostus speciosus rhizome essential oil against the Old-World bollworm, Helicoverpa armigera, Ecotoxicol. Environ. Saf., 148, 781–786, https://doi.org/10.1016/j.ecoenv.2017.11.044, 2018.

585 Bianchi, F., Kurtén, T., Riva, M., Mohr, C., Rissanen, M. P., Roldin, P., Berndt, T., Crounse, J. D., Wennberg, P. O., Mentel, T. F., Wildt, J., Junninen, H., Jokinen, T., Kulmala, M., Worsnop, D. R., Thornton, J. A., Donahue, N., Kjaergaard, H. G., and Ehn, M.: Highly Oxygenated Organic Molecules (HOM) from Gas-Phase Autoxidation Involving Peroxy Radicals: A Key Contributor to Atmospheric Aerosol, https://doi.org/10.1021/acs.chemrev.8b00395, 27 March 2019.

590 Camredon, M., Aumont, B., Lee-Taylor, J., and Madronich, S.: The SOA/VOC/NOx system: An explicit model of secondary organic aerosol formation, Atmos. Chem. Phys., https://doi.org/10.5194/acp-7-5599-2007, 2007.

Canagaratna, M. R., Jimenez, J. L., Kroll, J. H., Chen, Q., Kessler, S. H., Massoli, P., Hildebrandt Ruiz, L., Fortner, E., Williams, L. R., Wilson, K. R., Surratt, J. D., Donahue, N. M., Jayne, J. T., and Worsnop, D. R.: Elemental ratio measurements of organic compounds using aerosol mass spectrometry: Characterization, improved calibration, and
595 implications, Atmos. Chem. Phys., 15, 253–272, https://doi.org/10.5194/acp-15-253-2015, 2015.

Carter, W. P. L.: A detailed mechanism for the gas-phase atmospheric reactions of organic compounds, Atmos. Environ. Part A, Gen. Top., 24, 481–518, https://doi.org/10.1016/0960-1686(90)90005-8, 1990.

Carter, W. P. L.: Development of ozone reactivity scales for volatile organic compounds, J. Air Waste Manag. Assoc., 44, 881–899, https://doi.org/10.1080/1073161x.1994.10467290, 1994.

600   Carter, W. P. L. Documentation of the SAPRC-99 Chemical Mechanism for VOC Reactivity Assessment, 1999; p 329.

Carter, W. P. L.: Documentation of the SAPRC-99 Chemical Mechanism for VOC Reactivity Assessment, Report to the California Air Resources Board. Available at http://cert.ucr.edu/~carter/absts.htm#saprc99 and http://www.cert.ucr.edu/~carter/reactdat.htm., 2000.

605   Carter, W. P. L. Development of the SAPRC-07 Chemical Mechanism and Updated Ozone Reactivity Scales; Final Report to the California Air Resources Board Contract No. 03-318, March 2009.

Carter, W. P. L.: Development of a condensed SAPRC-07 chemical mechanism, Atmos. Environ., 44, 5336–5345, https://doi.org/10.1016/j.atmosenv.2010.01.024, 2010a.

Carter, W. P. L.: Development of the SAPRC-07 Chemical Mechanism and Updated Ozone Reactivity Scales, 2010b.

610   Carter, W. P. L.: Documentation of the SAPRC-18 Mechanism; Report to California Air Resources Board Contract No. 11-761, May, 2020. [online] Available from: https://intra.engr.ucr.edu/~carter/SAPRC/18/, 2020a.

Carter, W. P. L.: Gateway to the SAPRC Mechanism Generation System: http://mechgen.cert.ucr.edu/, last access: 30 March 2021.

Carter, W. P. L.: Estimates and Assignments used in the SAPRC-18 Mechanism Generation System; Report to
615   California Air Resources Board Contract No. 11-761. In preparation. When completed, will be available at http://intra.engr.ucr.edu/~carter/SAPRC/18, 2020b.

Carter, W. P. L. and Lurmann, F.W., 1990. Evaluation of the RADM gas-phase chemical mechanism. US Environmental Protection Agency, Atmospheric Research and Exposure Assessment Laboratory, Office of Research and Development.

620   Carter, W. P. L., Cocker, D. R., Fitz, D. R., Malkina, I. L., Bumiller, K., Sauer, C. G., Pisano, J. T., Bufalino, C., and Song, C.: A new environmental chamber for evaluation of gas-phase chemical mechanisms and secondary aerosol formation, Atmos. Environ., 39, 7768–7788, https://doi.org/10.1016/j.atmosenv.2005.08.040, 2005.

Clark, C. H., Kacarab, M., Nakao, S., Asa-Awuku, A., Sato, K., and Cocker, D. R.: Temperature Effects on Secondary Organic Aerosol (SOA) from the Dark Ozonolysis and Photo-Oxidation of Isoprene, Environ. Sci. Technol., 50,
625   5564–5571, https://doi.org/10.1021/acs.est.5b05524, 2016.

Cocker, D. R., Flagan, R. C., and Seinfeld, J. H.: State-of-the-art chamber facility for studying atmospheric aerosol chemistry, Environ. Sci. Technol., 35, 2594–2601, https://doi.org/10.1021/es0019169, 2001.

Crounse, J. D., Nielsen, L. B., Jørgensen, S., Kjaergaard, H. G., and Wennberg, P. O.: Autoxidation of Organic Compounds in the Atmosphere, J. Phys. Chem. Lett., 4, 3513–3520, https://doi.org/10.1021/JZ4019207, 2013.

630   DeCarlo, P. F., Kimmel, J. R., Trimborn, A., Northway, M. J., Jayne, J. T., Aiken, A. C., Gonin, M., Fuhrer, K., Horvath, T., Docherty, K. S., Worsnop, D. R., and Jimenez, J. L.: Field-deployable, high-resolution, time-of-flight aerosol mass spectrometer, Anal. Chem., 78, 8281–8289, https://doi.org/10.1021/ac061249n, 2006.

Donahue, N. -M., Robinson, A. L., Stanier, C. O., and Pandis, S. N.: Coupled partitioning, dilution, and chemical aging of semivolatile organics, Environ. Sci. Technol., 40, 2635–2643, https://doi.org/10.1021/es052297c, 2006.

635 Donahue, N. M., Robinson, A. L., and Pandis, S. N.: Atmospheric organic particulate matter: From smoke to secondary organic aerosol, Atmos. Environ., 43, 94–106, https://doi.org/10.1016/j.atmosenv.2008.09.055, 2009.

Eddingsaas, N. C., Loza, C. L., Yee, L. D., Chan, M., Schilling, K. A., Chhabra, P. S., Seinfeld, J. H., and Wennberg, P. O.: α-pinene photooxidation under controlled chemical conditions-Part 2: SOA yield and composition in low- and high-NO x environments, Atmos. Chem. Phys., 12, 7413–7427, https://doi.org/10.5194/acp-12-7413-2012,
640 2012.

Ehn, M., Berndt, T., Wildt, J., and Mentel, T.: Highly Oxygenated Molecules from Atmospheric Autoxidation of Hydrocarbons: A Prominent Challenge for Chemical Kinetics Studies, Int. J. Chem. Kinet., 49, 821–831, https://doi.org/10.1002/KIN.21130, 2017.

Fry, J. L., Draper, D. C., Barsanti, K. C., Smith, J. N., Ortega, J., Winkler, P. M., Lawler, M. J., Brown, S. S., Edwards,
645 P. M., Cohen, R. C., and Lee, L.: Secondary Organic Aerosol Formation and Organic Nitrate Yield from NO 3 Oxidation of Biogenic Hydrocarbons Terms of Use CC-BY, Environ. Sci. Technol, 48, https://doi.org/10.1021/es502204x, 2014.

Gaona-Colmán, E., Blanco, M. B., Barnes, I., Wiesen, P., and Teruel, M. A.: OH- and O3-initiated atmospheric degradation of camphene: temperature dependent rate coefficients, product yields and mechanisms, RSC Adv., 7,
650 2733–2744, https://doi.org/10.1039/c6ra26656h, 2017.

Geron, C., Rasmussen, R., Arnts, R. R., and Guenther, A.: A review and synthesis of monoterpene speciation from forests in the United States, Atmos. Environ., https://doi.org/10.1016/S1352-2310(99)00364-7, 2000.

Gilman, J. B., Lerner, B. M., Kuster, W. C., Goldan, P. D., Warneke, C., Veres, P. R., Roberts, J. M., De Gouw, J. A., Burling, I. R., and Yokelson, R. J.: Biomass burning emissions and potential air quality impacts of volatile organic
655 compounds and other trace gases from fuels common in the US, Atmos. Chem. Phys., https://doi.org/10.5194/acp-15-13915-2015, 2015.

Griffin, R. J., Cocker, D. R., Flagan, R. C., and Seinfeld, J. H.: Organic aerosol formation from the oxidation of biogenic hydrocarbons, J. Geophys. Res. Atmos., https://doi.org/10.1029/1998JD100049, 1999.

Guenther, A.: A global model of natural volatile organic compound emissions, J. Geophys. Res.,
660 https://doi.org/10.1029/94JD02950, 1995.

Hakola, H., Arey, J., Aschmann, S. M., and Atkinson, R.: Product formation from the gas-phase reactions of OH radicals and O3 with a series of monoterpenes, J. Atmos. Chem., https://doi.org/10.1007/BF00694375, 1994.

Hatch, L. E., Luo, W., Pankow, J. F., Yokelson, R. J., Stockwell, C. E., and Barsanti, K. C.: Identification and quantification of gaseous organic compounds emitted from biomass burning using two-dimensional gas
665 chromatography-time-of-flight mass spectrometry, Atmos. Chem. Phys., https://doi.org/10.5194/acp-15-1865-2015, 2015.

Hatch, L. E., Jen, C. N., Kreisberg, N. M., Selimovic, V., Yokelson, R. J., Stamatis, C., York, R. A., Foster, D., Stephens, S. L., Goldstein, A. H., and Barsanti, K. C.: Highly Speciated Measurements of Terpenoids Emitted from

Laboratory and Mixed-Conifer Forest Prescribed Fires, Environ. Sci. Technol., https://doi.org/10.1021/acs.est.9b02612, 2019.

Hatfield, M. L. and Huff Hartz, K. E.: Secondary organic aerosol from biogenic volatile organic compound mixtures, Atmos. Environ., 45, 2211–2219, https://doi.org/10.1016/j.atmosenv.2011.01.065, 2011.

Hayward, S., Muncey, R. J., James, A. E., Halsall, C. J., and Hewitt, C. N.: Monoterpene emissions from soil in a Sitka spruce forest, Atmos. Environ., https://doi.org/10.1016/S1352-2310(01)00213-8, 2001.

Henze, D. K., Seinfeld, J. H., Ng, N. L., Kroll, J. H., Fu, T. M., Jacob, D. J., and Heald, C. L.: Global modeling of secondary organic aerosol formation from aromatic hydrocarbons: High- vs. low-yield pathways, Atmos. Chem. Phys., 8, 2405–2421, https://doi.org/10.5194/acp-8-2405-2008, 2008.

Hurley, M. D., Sokolov, O., and Wallington, T. J.: Organic aerosol formation during the atmospheric degradation of toluene, Environ. Sci. Technol., 35, 1358–1366, https://doi.org/10.1021/es0013733, 2001.

Jay R. Odum, Thorsten Hoffmann, Frank Bowman, Don Collins, Richard C. Flagan, and John H. Seinfeld: Gas/Particle Partitioning and Secondary Organic Aerosol Yields, 2580–2585 pp., https://doi.org/10.1021/ES950943, 1996.

Jiang, J., Carter, W. P. L., Cocker, D. R., and Barsanti, K. C.: Development and Evaluation of a Detailed Mechanism for Gas-Phase Atmospheric Reactions of Furans, ACS Earth Sp. Chem., 4, 1254–1268, https://doi.org/10.1021/acsearthspacechem.0c00058, 2020a.

Jiang, J., Carter, W. P. L., Cocker, D. R., and Barsanti, K. C.: Development and Evaluation of a Detailed Mechanism for Gas-Phase Atmospheric Reactions of Furans, ACS Earth Sp. Chem., 4, 1254–1268, https://doi.org/10.1021/acsearthspacechem.0c00058, 2020b.

Jokinen, T., Sipilä, M., Richters, S., Kerminen, V.-M., Paasonen, P., Stratmann, F., Worsnop, D., Kulmala, M., Ehn, M., Herrmann, H., and Berndt, T.: Rapid Autoxidation Forms Highly Oxidized RO2 Radicals in the Atmosphere, Angew. Chemie Int. Ed., 53, 14596–14600, https://doi.org/10.1002/ANIE.201408566, 2014.

Komenda, M.: Monoterpene emissions from Scots pine (*Pinus sylvestris*): Field studies of emission rate variabilities, J. Geophys. Res., 107, 4161, https://doi.org/10.1029/2001JD000691, 2002.

Kroll, J. H. and Seinfeld, J. H.: Chemistry of secondary organic aerosol: Formation and evolution of low-volatility organics in the atmosphere, https://doi.org/10.1016/j.atmosenv.2008.01.003, 1 May 2008.

Kroll, J. H., Ng, N. L., Murphy, S. M., Flagan, R. C., and Seinfeld, J. H.: Secondary organic aerosol formation from isoprene photooxidation, Environ. Sci. Technol., 40, 1869–1877, https://doi.org/10.1021/es0524301, 2006.

Kuwata, M., Zorn, S. R., and Martin, S. T.: Using elemental ratios to predict the density of organic material composed of carbon, hydrogen, and oxygen, Environ. Sci. Technol., 46, 787–794, https://doi.org/10.1021/es202525q, 2012.

Lannuque, V., Camredon, M., Couvidat, F., Hodzic, A., Valorso, R., Madronich, S., Bessagnet, B., and Aumont, B.: Exploration of the influence of environmental conditions on secondary organic aerosol formation and organic species properties using explicit simulations: Development of the VBS-GECKO parameterization, Atmos. Chem. Phys., 18, 13411–13428, https://doi.org/10.5194/acp-18-13411-2018, 2018.

Li, L., Tang, P., and Cocker, D. R.: Instantaneous nitric oxide effect on secondary organic aerosol formation from m-xylene photooxidation, Atmos. Environ., 119, 144–155, https://doi.org/10.1016/j.atmosenv.2015.08.010, 2015.

Li, L., Tang, P., Nakao, S., and Cocker, D. R.: Impact of molecular structure on secondary organic aerosol formation from aromatic hydrocarbon photooxidation under low-NOx conditions, Atmos. Chem. Phys., 16, 10793–10808, https://doi.org/10.5194/ACP-16-10793-2016, 2016.

Li, Q., Hu, D., Leungsakul, S., and Kamens, R. M.: Large outdoor chamber experiments and computer simulations: (I) Secondary organic aerosol formation from the oxidation of a mixture of d-limonene and α-pinene, Atmos. Environ., 41, 9341–9352, https://doi.org/10.1016/j.atmosenv.2007.09.017, 2007.

Ludley, K. E., Jickells, S. M., Chamberlain, P. M., Whitaker, J., and Robinson, C. H.: Distribution of monoterpenes between organic resources in upper soil horizons under monocultures of Picea abies, Picea sitchensis and Pinus sylvestris, Soil Biol. Biochem., https://doi.org/10.1016/j.soilbio.2009.02.002, 2009.

Maleknia, S. D., Bell, T. L., and Adams, M. A.: PTR-MS analysis of reference and plant-emitted volatile organic compounds, Int. J. Mass Spectrom., https://doi.org/10.1016/j.ijms.2006.11.010, 2007.

Malloy, Q. G. J., Nakao, S., Qi, L., Austin, R., Stothers, C., Hagino, H., and Cocker, D. R.: Real-Time aerosol density determination utilizing a modified scanning mobility particle sizer aerosol particle mass analyzer system, Aerosol Sci. Technol., 43, 673–678, https://doi.org/10.1080/02786820902832960, 2009.

Mazza, G. and Cottrell, T.: Volatile components of roots, stems, leaves, and flowers of Echinacea species, J. Agric. Food Chem., https://doi.org/10.1021/jf981117y, 1999.

McVay, R. C., Zhang, X., Aumont, B., Valorso, R., Camredon, M., La, Y. S., Wennberg, P. O., and Seinfeld, J. H.: SOA formation from the photooxidation of α-pinene: Systematic exploration of the simulation of chamber data, Atmos. Chem. Phys., 16, 2785–2802, https://doi.org/10.5194/acp-16-2785-2016, 2016.

Mehra, A., Krechmer, J. E., Lambe, A., Sarkar, C., Williams, L., Khalaj, F., Guenther, A., Jayne, J., Coe, H., Worsnop, D., Faiola, C., and Canagaratna, M.: Oligomer and highly oxygenated organic molecule formation from oxidation of oxygenated monoterpenes emitted by California sage plants, Atmos. Chem. Phys., 20, 10953–10965, https://doi.org/10.5194/acp-20-10953-2020, 2020.

Moukhtar, S., Couret, C., Rouil, L., and Simon, V.: Biogenic Volatile Organic Compounds (BVOCs) emissions from Abies alba in a French forest, Sci. Total Environ., 354, 232–245, https://doi.org/10.1016/j.scitotenv.2005.01.044, 2006.

Mutzel, A., Rodigast, M., Iinuma, Y., Böge, O., and Herrmann, H.: Monoterpene SOA - Contribution of first-generation oxidation products to formation and chemical composition, Atmos. Environ., 130, 136–144, https://doi.org/10.1016/j.atmosenv.2015.10.080, 2016.

Nakao, S., Tang, P., Tang, X., Clark, C. H., Qi, L., Seo, E., Asa-Awuku, A., and Cocker, D.: Density and elemental ratios of secondary organic aerosol: Application of a density prediction method, Atmos. Environ., 68, 273–277, https://doi.org/10.1016/j.atmosenv.2012.11.006, 2013.

Nannoolal, Y., Rarey, J., and Ramjugernath, D.: Estimation of pure component properties part 3. Estimation of the vapor pressure of non-electrolyte organic compounds via group contribution and group interactions, Fluid Phase Equilib., 269, 117–133, https://doi.org/10.1016/j.fluid.2008.04.020, 2008.

Ng, N. L., Chhabra, P. S., Chan, A. W. H., Surratt, J. D., Kroll, J. H., Kwan, A. J., McCabe, D. C., Wennberg, P. O., Sorooshian, A., Murphy, S. M., Dalleska, N. F., Flagan, R. C., and Seinfeld, J. H.: Effect of NOx level on secondary

organic aerosol (SOA) formation from the photooxidation of terpenes, Atmos. Chem. Phys., 7, 5159–5174, https://doi.org/10.5194/acp-7-5159-2007, 2007a.

745   Ng, N. L., Chhabra, P. S., Chan, A. W. H., Surratt, J. D., Kroll, J. H., Kwan, A. J., McCabe, D. C., Wennberg, P. O., Sorooshian, A., Murphy, S. M., Dalleska, N. F., Flagan, R. C., and Seinfeld, J. H.: Effect of NOx level on secondary organic aerosol (SOA) formation from the photooxidation of terpenes, Atmos. Chem. Phys., https://doi.org/10.5194/acp-7-5159-2007, 2007b.

Nøjgaard, J. K., Bilde, M., Stenby, C., Nielsen, O. J., and Wolkoff, P.: The effect of nitrogen dioxide on particle
750   formation during ozonolysis of two abundant monoterpenes indoors, Atmos. Environ., 40, 1030–1042, https://doi.org/10.1016/j.atmosenv.2005.11.029, 2006.

Pankow, J. F.: An absorption model of the gas/aerosol partitioning involved in the formation of secondary organic aerosol, Atmos. Environ., 41, 75–79, https://doi.org/10.1016/j.atmosenv.2007.10.060, 1994.

Presto, A. A., Huff Hartz, K. E., and Donahue, N. M.: Secondary organic aerosol production from terpene ozonolysis.
755   2. Effect of NOx concentration, Environ. Sci. Technol., 39, 7046–7054, https://doi.org/10.1021/es050400s, 2005.

Pullinen, I., Schmitt, S., Kang, S., Sarrafzadeh, M., Schlag, P., Andres, S., Kleist, E., Mentel, T. F., Rohrer, F., Springer, M., Tillmann, R., Wildt, J., Wu, C., Zhao, D., Wahner, A., and Kiendler-Scharr, A.: Impact of NOx on secondary organic aerosol (SOA) formation from α-pinene and β-pinene photooxidation: The role of highly oxygenated organic nitrates, Atmos. Chem. Phys., 20, 10125–10147, https://doi.org/10.5194/acp-20-10125-2020, 2020.

760   Pye, H. O. T., Chan, A. W. H., Barkley, M. P., and Seinfeld, J. H.: Global modeling of organic aerosol: The importance of reactive nitrogen (NOx and NO3), Atmos. Chem. Phys., 10, 11261–11276, https://doi.org/10.5194/ACP-10-11261-2010, 2010.

Pye, H. O. T., D'Ambro, E. L., Lee, B. H., Schobesberger, S., Takeuchi, M., Zhao, Y., Lopez-Hilfiker, F., Liu, J., Shilling, J. E., Xing, J., Mathur, R., Middlebrook, A. M., Liao, J., Welti, A., Graus, M., Warneke, C., de Gouw, J.
765   A., Holloway, J. S., Ryerson, T. B., Pollack, I. B., and Thornton, J. A.: Anthropogenic enhancements to production of highly oxygenated molecules from autoxidation, Proc. Natl. Acad. Sci. U. S. A., 116, 6641–6646, https://doi.org/10.1073/pnas.1810774116, 2019.

Quéléver, L. L. J., Kristensen, K., Jensen, L. N., Rosati, B., Teiwes, R., Daellenbach, K. R., Peräkylä, O., Roldin, P., Bossi, R., Pedersen, H. B., Glasius, M., Bilde, M., and Ehn, M.: Effect of temperature on the formation of highly
770   oxygenated organic molecules (HOMs) from alpha-pinene ozonolysis, Atmos. Chem. Phys., 19, 7609–7625, https://doi.org/10.5194/ACP-19-7609-2019, 2019.

Sarrafzadeh, M., Wildt, J., Pullinen, I., Springer, M., Kleist, E., Tillmann, R., Schmitt, S. H., Wu, C., Mentel, T. F., Zhao, D., Hastie, D. R., and Kiendler-Scharr, A.: Impact of NOx and OH on secondary organic aerosol formation from β-pinene photooxidation, Atmos. Chem. Phys., 16, 11237–11248, https://doi.org/10.5194/acp-16-11237-2016,
775   2016.

Schervish, M. and Donahue, N. M.: Peroxy radical chemistry and the volatility basis set, Atmos. Chem. Phys., 20, 1183–1199, https://doi.org/10.5194/acp-20-1183-2020, 2020.

Schwantes, R. H., Charan, S. M., Bates, K. H., Huang, Y., Nguyen, T. B., Mai, H., Kong, W., Flagan, R. C., and Seinfeld, J. H.: Low-volatility compounds contribute significantly to isoprene secondary organic aerosol (SOA)

under high-NOx conditions, Atmos. Chem. Phys., 19, 7255–7278, https://doi.org/10.5194/ACP-19-7255-2019, 2019.

Song, C., Na, K., and Cocker, D. R.: Impact of the hydrocarbon to NOx ratio on secondary organic aerosol formation, Environ. Sci. Technol., https://doi.org/10.1021/es0493244, 2005.

White, M. L., Russo, R. S., Zhou, Y., Mao, H., Varner, R. K., Ambrose, J., Veres, P., Wingenter, O. W., Haase, K., Stutz, J., Talbot, R., and Sive, B. C.: Volatile organic compounds in northern New England marine and continental environments during the ICARTT 2004 campaign, J. Geophys. Res. Atmos., https://doi.org/10.1029/2007JD009161, 2008.

Xavier, C., Rusanen, A., Zhou, P., Dean, C., Pichelstorfer, L., Roldin, P., and Boy, M.: Aerosol mass yields of selected biogenic volatile organic compounds - A theoretical study with nearly explicit gas-phase chemistry, Atmos. Chem. Phys., 19, 13741–13758, https://doi.org/10.5194/ACP-19-13741-2019, 2019.

Ye, Q., Wang, M., Hofbauer, V., Stolzenburg, D., Chen, D., Schervish, M., Vogel, A., Mauldin, R.L., Baalbaki, R., Brilke, S., and Dada, L.: Molecular Composition and Volatility of Nucleated Particles from α-Pinene Oxidation between -50 °C and +25 °C, Environ. Sci. Technol., 53, 12357–12365, https://doi.org/10.1021/ACS.EST.9B03265, 2019.

Zhang, S.-H., Shaw, M., Seinfeld, J. H., and Flagan, R. C.: Photochemical Aerosol Formation From c-Pinene-and 13-Pinene, JOURNAL OF GEOPHYSICAL RESEARCH, 717–737 pp., 1992.

Zhang, X., Cappa, C. D., Jathar, S. H., McVay, R. C., Ensberg, J. J., Kleeman, M. J., and Seinfeld, J. H.: Influence of vapor wall loss in laboratory chambers on yields of secondary organic aerosol, Proc. Natl. Acad. Sci., 111, 5802–5807, https://doi.org/10.1073/PNAS.1404727111, 2014.

Zhang, X., Lambe, A. T., Upshur, M. A., Brooks, W. A., Bé, A. G., Thomson, R. J., Geiger, F. M., Surratt, J. D., Zhang, Z., Gold, A., Graf, S., Cubison, M. J., Groessl, M., Jayne, J. T., Worsnop, D. R., and Canagaratna, M. R.: Highly Oxygenated Multifunctional Compounds in α-Pinene Secondary Organic Aerosol, Environ. Sci. Technol., 51, 5932–5940, https://doi.org/10.1021/ACS.EST.6B06588, 2017.

Zhang, X., Schwantes, R. H., McVay, R. C., Lignell, H., Coggon, M. M., Flagan, R. C., and Seinfeld, J. H.: Vapor wall deposition in Teflon chambers, Atmos. Chem. Phys., 15, 4197–4214, https://doi.org/10.5194/ACP-15-4197-2015, 2015.

Zhao, Y., Thornton, J. A., and Pye, H. O. T.: Quantitative constraints on autoxidation and dimer formation from direct probing of monoterpene-derived peroxy radical chemistry, Proc. Natl. Acad. Sci. U. S. A., 115, 12142–12147, https://doi.org/10.1073/pnas.1812147115, 2018.

Ziemann, P. J. and Atkinson, R.: Kinetics, products, and mechanisms of secondary organic aerosol formation, Chem. Soc. Rev., 41, 6582–6605, https://doi.org/10.1039/c2cs35122f, 2012.